The Astrophysical Journal, 892:97 (17pp), 2020 April 1 https://doi.org/10.3847/1538-4357/ab7248

Lowly Polarized Light from a Highly Magnetized Jet of GRB 190114C

N. Jordana-Mitjans[1], C. G. Mundell[1], S. Kobayashi[2], R. J. Smith[2], C. Guidorzi[3], I. A. Steele[2], M. Shrestha[2], A. Gomboc[4], M. Marongiu[3,5], R. Martone[3,5], V. Lipunov[6], E. S. Gorbovskoy[6], D. A. H. Buckley[7], R. Rebolo[8], and N. M. Budnev[9]

[1] Department of Physics, University of Bath, Claverton Down, Bath, BA2 7AY, UK; N.Jordana@bath.ac.uk
[2] Astrophysics Research Institute, Liverpool John Moores University, 146 Brownlow Hill, Liverpool, L3 5RF, UK
[3] Department of Physics and Earth Science, University of Ferrara, via Saragat 1, I-44122, Ferrara, Italy
[4] Center for Astrophysics and Cosmology, University of Nova Gorica, Vipavska 13, 5000 Nova Gorica, Slovenia
[5] ICRANet, Piazzale della Repubblica 10, I-65122, Pescara, Italy
[6] Lomonosov Moscow State University, SAI, Physics Department, 13 Univeristetskij pr-t, Moscow 119991, Russia
[7] South African Astronomical Observatory, P.O. Box 9, Observatory 7935, Cape Town, South Africa
[8] Instituto de Astrofísica de Canarias (IAC), Calle Vía Láctea s/n, E-38200 La Laguna, Tenerife, Spain
[9] Applied Physics Institute, Irkutsk State University, 20 Gagarin Blvd., 664003, Irkutsk, Russia
Received 2019 November 8; revised 2020 January 18; accepted 2020 February 1; published 2020 April 2

Abstract

We report multicolor optical imaging and polarimetry observations of the afterglow of the first TeV-detected gamma-ray burst (GRB), GRB 190114C, using the RINGO3 and MASTER II polarimeters. Observations begin 31 s after the onset of the GRB and continue until ∼7000 s postburst. The light curves reveal a chromatic break at ∼400–500 s, with initial temporal decay $\alpha = 1.669 \pm 0.013$ flattening to $\alpha \sim 1$ postbreak, which we model as a combination of reverse and forward shock components with magnetization parameter $R_B \sim 70$. The observed polarization degree decreases from $7.7\% \pm 1.1\%$ to 2%–4% 52–109 s postburst and remains steady at this level for the subsequent ∼2000 s at a constant position angle. Broadband spectral energy distribution modeling of the afterglow confirms that GRB 190114C is highly obscured ($A_{v,HG} = 1.49 \pm 0.12$ mag; $N_{H,HG} = (9.0 \pm 0.03) \times 10^{22}$ cm^{-2}). We interpret the measured afterglow polarization as intrinsically low and dominated by dust —in contrast to the $P > 10\%$ measured previously for other GRB reverse shocks—with a small contribution from polarized prompt photons in the first minute. We test whether first- and higher-order inverse Compton scattering in a magnetized reverse shock can explain the low optical polarization and subteraelectronvolt emission but conclude that neither is explained in the reverse shock inverse Compton model. Instead, the unexpectedly low intrinsic polarization degree in GRB 190114C can be explained if large-scale jet magnetic fields are distorted on timescales prior to reverse shock emission.

Unified Astronomy Thesaurus concepts: High energy astrophysics (739); Gamma-ray bursts (629); Magnetic fields (994); Polarimetry (1278); Shocks (2086); Jets (870); Photometric systems (1233)

Supporting material: machine-readable table

1. Introduction

Through the span of milliseconds to hundreds of seconds, gamma-ray bursts (GRBs) are the brightest sources of γ-ray photons in the universe. The accretion onto a compact object (e.g., a neutron star or black hole) powers ultrarelativistic jets that, via internal dissipation processes (e.g., internal shocks or magnetic reconnection), generate the characteristic and variable γ-ray prompt emission. Subsequently, the expanding ejecta collides with the circumburst medium, producing a long-lived afterglow that can be detected at wavelengths across the electromagnetic spectrum (e.g., Piran 1999; Mészáros 2002; Piran 2004).

The GRB outflows provide a unique opportunity to probe the nature of GRB progenitors, thought to involve the core collapse of massive stars or the merger of compact stellar objects (Woosley 1993; Berger 2014; Abbott et al. 2017b, 2017a), as well as acting as valuable laboratories for the study of relativistic jet physics (e.g., jet composition, energy dissipation, shock physics, and radiation emission mechanisms) and their environments.

At the onset of the afterglow, two shocks develop: a forward shock that travels into the external medium and a short-lived reverse shock that propagates back into the jet (Sari & Piran 1999; Kobayashi 2000). The interaction between the outflow and the ambient medium can be quantified by the magnetization degree of the ejecta σ_B, defined as the ratio of magnetic to kinetic energy flux. In a matter-dominated regime ($\sigma_B \ll 1$; baryonic jet), the standard fireball model conditions are satisfied and internal shocks are plasma-dominated (Rees & Meszaros 1994). For increasing σ_B, the reverse shock becomes stronger until it reaches a maximum at $\sigma_B \sim 0.1$, and it becomes progressively weaker and likely suppressed for $\sigma_B \gtrsim 1$ (Zhang et al. 2003; Fan et al. 2004; Zhang & Kobayashi 2005; Giannios et al. 2008). For an outflow highly magnetized at the deceleration radius ($\sigma_B \gg 1$; Poynting flux jet), the magnetic fields are dynamically dominant, prompt emission is understood in terms of magnetic dissipation processes, and the ejecta carries globally ordered magnetic fields (Usov 1994; Spruit et al. 2001; Lyutikov & Blandford 2003).

Observations of the optical afterglow show low or no polarization at late times (∼1 day) when the forward shock—powered by a shocked ambient medium—dominates the light curve (e.g., Covino et al. 1999). In contrast, the prompt and early-time afterglow emission from the reverse shock are sensitive to the properties of the central engine ejecta. At this stage, different polarization signatures are predicted for magnetic and baryonic jet models. In a Poynting flux–dominated jet, the early-time emission is expected to be highly polarized due to the presence of primordial magnetic fields advected from the central engine (Granot & Königl 2003;

Lyutikov et al. 2003; Fan et al. 2004; Zhang & Kobayashi 2005). In a baryonic jet, tangled magnetic fields locally generated in shocks are randomly oriented in space, giving rise to unpolarized emission for on-axis jets (Medvedev & Loeb 1999) or mild polarization detections for edge-on jets (Ghisellini & Lazzati 1999; Sari 1999). Therefore, early-time polarization measurements of the afterglow are crucial for diagnosing its composition and discriminating between competing jet models.

Polarization measurements are technically challenging, and reverse shock detections remain rare (e.g., Japelj et al. 2014). However, the advent of autonomous optical robotic telescopes and real-time arcminute localization of GRBs has made these observations feasible (Steele et al. 2004; Barthelmy et al. 2005).

The first early-time polarization measurement in the optical was achieved with GRB 060418 (Mundell et al. 2007). The fast response of the polarimeter allowed observations during the deceleration of the blast wave, beginning 203 s after the GRB. The upper limit of 8% at this time either favored reverse shock suppression due to a highly magnetized ejecta or ruled out the presence of large-scale ordered magnetic fields with dominant reverse shock emission.

The measurement of $10\% \pm 1\%$ during the steep decay of the GRB 090102 reverse shock—measured only 160 s postburst—was the first evidence that large-scale ordered magnetic fields are present in the fireball (Steele et al. 2009). The $6^{+3}_{-2}\%$ and $6^{+4}_{-3}\%$ detection during the rise and decay of the GRB 101112A afterglow and the $13^{+13}_{-9}\%$ measurement during the rapid rise of the GRB 110205A afterglow indicated reverse shock contribution (Cucchiara et al. 2011; Steele et al. 2017). The GRB 120308A polarization gradual decrease from $28\% \pm 4\%$ to $16^{+5}_{-4}\%$ revealed that these large-scale fields could survive long after the deceleration of the fireball (Mundell et al. 2013). The time-sampled polarimetry for both GRB 101112A and GRB 120308A indicated that the polarization position angle remained constant or rotated only gradually, consistent with stable, globally ordered magnetic fields in a relativistic jet. The first detection of polarized prompt optical emission was reported by Troja et al. (2017) for GRB 160625B.

In combination, the existence of bright reverse shock emission theoretically requires a mildly magnetized jet, and the early-time polarization studies favor the presence of primordial magnetic fields advected from the central engine.

The GRB 190114C is the first of its kind to be detected by the Major Atmospheric Gamma Imaging Cherenkov Telescope (MAGIC) at subteraelectronvolt energies (Mirzoyan 2019), challenging GRB models for the production of GeV–TeV energies (Ajello et al. 2020; Derishev & Piran 2019; Fraija et al. 2019a; Ravasio et al. 2019; Wang et al. 2019; MAGIC Collaboration et al. 2019a; MAGIC Collaboration et al. 2019b). Moreover, GRB 190114C prompt emission was followed by a very bright afterglow, which makes it an interesting candidate for time-resolved polarimetric observations at early times (Mundell et al. 2013; Steele et al. 2017; Troja et al. 2017).

In this work, we present the early-time multicolor optical imaging polarimetric observations of GRB 190114C with the RINGO3 three-band imaging polarimeter (Arnold et al. 2012) mounted on the 2 m autonomous robotic optical Liverpool Telescope (LT; Steele et al. 2004; Guidorzi et al. 2006) and the fully robotic 0.4 m MASTER–SAAO/IAC II telescopes from the MASTER Global Robotic Net (Lipunov et al. 2010; Kornilov et al. 2012). The paper is structured as follows. The data reduction of the LT and MASTER observations is reported in Section 2. In Section 3, we characterize the temporal, polarimetric, and spectral properties of the burst in three optical bands with observations starting 201 s postburst and a white band since 30.7 s. In Section 4, we model the optical afterglow with a reverse–forward shock model. In Section 5, we discuss reverse shock synchrotron self-Compton (SSC) as a possible mechanism for the sub-TeV detection, and we infer the strength and structure of the magnetic field in the outflow. The results are summarized in Section 6. Throughout this work, we assume a flat ΛCDM cosmology, $\Omega_{\rm m} = 0.32$, $\Omega_\Lambda = 0.68$, and $h = 0.67$, as reported by Planck Collaboration et al. (2018). We adopt the convention $F_\nu \propto t^{-\alpha}\ \nu^{-\beta}$, where α is the temporal index and β is the spectral index. Uncertainties are quoted at a 1σ confidence level unless stated otherwise.

2. Observations and Data Reduction

On 2019 January 14 at $T_0 = 20{:}57{:}03$ UT, the *Swift* Burst Alert Telescope (BAT; Barthelmy et al. 2005) triggered an alert for the GRB candidate 190114C and immediately slewed toward its position (Gropp et al. 2019). Other telescopes also reported the detection of the GRB 190114C γ-ray prompt as a multipeaked structure: Konus-*Wind* (KW; Frederiks et al. 2019), the *Fermi* Gamma-ray Burst Monitor (GBM; Hamburg et al. 2019), the *Fermi* Large Area Telescope (LAT; Kocevski et al. 2019), *Astro-Rivelatore Gamma a Immagini Leggero* (*AGILE*; Ursi et al. 2019), the *International Gamma-Ray Astrophysics Laboratory* (Minaev & Pozanenko 2019), and the *Hard X-ray Modulation Telescope* (*Insight-HXMT/HE*; Xiao et al. 2019). At $T_0 + 50$ s, MAGIC detected the burst at energies higher than 300 GeV with a significance of $>20\sigma$ (Mirzoyan 2019).

Due to the different spectral coverage of the detectors and the presence of soft extended emission (Frederiks et al. 2019; Hamburg et al. 2019; Minaev & Pozanenko 2019), the long γ-ray prompt was observed to last $T_{90} = 362 \pm 12$ s in the 15–350 keV band (BAT; Krimm et al. 2019), $T_{90} = 116$ s in the 50–300 keV band (GBM; Hamburg et al. 2019), $T_{90} = 15.7$ s in the 200–3000 keV band (*Insight-HXMT/HE*; Xiao et al. 2019), and $T_{90} = 6.2$ s in the 0.4–100 MeV band (*AGILE*; Ursi et al. 2019). The KW analysis reported an energy peak $E_{\rm peak} = 646 \pm 16$ keV, an isotropic energy $E_{\rm iso} = (2.40 \pm 0.05) \times 10^{53}$ erg, and a peak luminosity $L_{\rm iso} = (1.67 \pm 0.05) \times 10^{53}$ erg s^{-1} and pointed out that these values follow the Amati–Yonetoku relation within 1σ (Frederiks et al. 2019).

Seconds to days after the burst, GRB 190114C afterglow was observed at wavelengths from the X-ray to the infrared (see Figure 1 and references therein) and down to radio frequencies (Alexander et al. 2019; Cherukuri et al. 2019; Laskar et al. 2019a, 2019b; Schulze et al. 2019; Volvach et al. 2019; Tremou et al. 2019). The fastest response to the BAT trigger was from the MASTER–SAAO Very Wide-Field (VWF) camera at $T_0 + 30.7$ s with an $\sim 10.51 \pm 0.12$ mag detection in the optical (see Section 2.2). Later observations started at $T_0 + 67$, 74, and 201 s with the *Swift* X-ray Telescope (XRT; D'Elia et al. 2019), 0.3 m Ultraviolet/Optical Telescope (UVOT; Siegel & Gropp 2019), and 2 m LT (see Section 2.1), respectively. A spectroscopic redshift of 0.4245 ± 0.0005 was measured by the 10.4 m Gran Telescopio

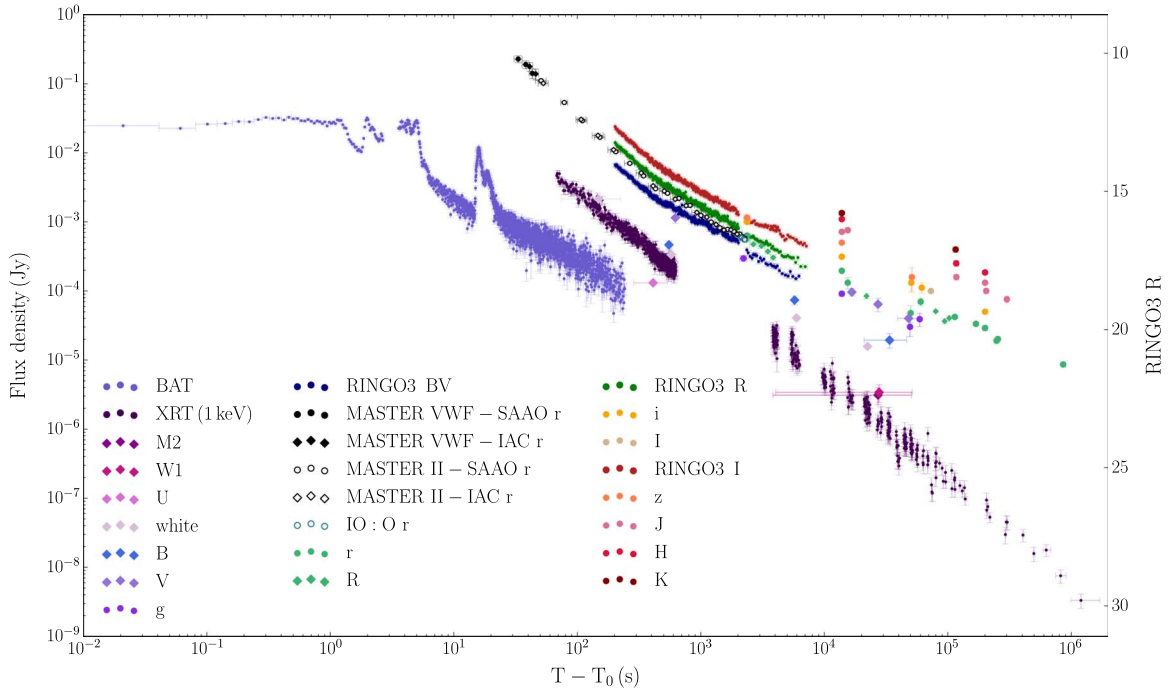

Figure 1. The GRB 190114C multiwavelength light curves with the *Swift* BAT, *Swift* XRT, MASTER–SAAO/IAC VWF *r*-equivalent, MASTER–SAAO/IAC II *r*-equivalent, LT RINGO3 *BV/R/I*, and LT IO:O *r* bands. *Swift* data are obtained from the web interface provided by Leicester University (Evans et al. 2009); BAT data are binned to a signal-to-noise ratio of 5, and the absorbed 0.3–10 keV XRT light curve is converted to flux density at 1 keV. For completeness, we include the UV/optical/infrared observations reported in GCNs from UVOT (Siegel & Gropp 2019), NOT (Selsing et al. 2019), OASDG (Izzo et al. 2019), GROND (Bolmer & Schady 2019), REM (D'Avanzo 2019), McDonald Observatory (Im et al. 2019a), LSGT (Kim & Im 2019), GRowth-India (Kumar et al. 2019b), KMTNet (Kim et al. 2019), UKIRT (Im et al. 2019b), CHILESCOPE (Mazaeva et al. 2019a, 2019b, 2019c), RTT150 (Bikmaev et al. 2019), ePESSTO NTT (Ragosta et al. 2019), RATIR (Watson et al. 2019), and HCT (Kumar et al. 2019a; Singh et al. 2019). The Gamma-ray Coordination Network (GCN) observations do not include filter corrections. In the *x*-axis, T_0 corresponds to BAT trigger time; in the *y*-axis, the flux density is converted to RINGO3 *R* magnitude.

Canarias and confirmed by the 2.5 m Nordic Optical Telescope (NOT; Castro-Tirado et al. 2019; Selsing et al. 2019). Additionally, a supernova component was detected 15 days after the burst, confirming a collapsar origin for GRB 190114C (Melandri et al. 2019).

2.1. Follow-up Observations by the LT

The 2 m robotic LT (Steele et al. 2004; Guidorzi et al. 2006) started observing the field 201 s after the burst with the multiwavelength imager and polarimeter RINGO3. For a typical GRB follow-up, the telescope autonomously schedules a series of 3 × 10 minute observations with RINGO3 followed by a 6 × 10 s sequence with the *r*-SDSS filter of the Optical Wide Field Camera[10] (IO:O). Due to GRB 190114C's exceptional brightness, an additional 8 × 10 minute integrations were triggered with RINGO3 after the IO:O observations.

RINGO3 is a fast-readout optical polarimeter that simultaneously provides polarimetry and imaging in three optical/infrared bands (Arnold et al. 2012). The instrument design includes a rotating polaroid that continuously images a $4' \times 4'$ field at eight rotor positions. Each RINGO3 10 minute primary data product is composed of 10 × 1 minute exposure frames. These frames are automatically generated by the LT reduction pipeline,[11] which coadds the individual 2.34 s frames that correspond to a single polaroid rotation and corrects for bias, darks, and flats. For photometry, we integrate the counts over all polaroid positions (see Section 2.1.1); for polarimetry, we analyze the relative intensity of the source at the eight angle positions of the polaroid (see Section 2.1.3).

2.1.1. Frame Binning and Three-band Light-curve Extraction

We use aperture photometry to compute the source flux; in particular, we employ the ASTROPY PHOTUTILS package (Bradley et al. 2016). The brightness of the optical transient (OT) during the RINGO3 observations provides a high signal-to-noise ratio even at high temporal resolution; the source is detected at a signal-to-noise ratio of $\gtrsim$60 in each of the first ∼10 × 2.34 s frames. Due to the fading nature of the afterglow, the signal-to-noise ratio of the detection rapidly drops for the following observations (e.g., 200 s later, the signal-to-noise ratio of each 2.34 s frame decreases to ∼30). By $\sim T_0 + 2000$ s, the source is detected in the 1 minute frames at a signal-to-noise ratio of ∼25. Consequently, our data choice is to use the 2.34 s RINGO3 frames for the first 30 minutes of observations to allow high temporal resolution, then the 1 minute exposures for the succeeding 1.3 hr.

At later times, when the OT has faded, we dynamically coadd frames and accept measurements with a $\geqslant$20 signal-to-noise ratio detection. With these signal-to-noise ratio criteria, $\gtrsim T_0 + 700$ s measurements are the result of coadding frames. Integrating at different signal-to-noise ratios does not change the light-curve general features: $\ll$20 signal-to-noise ratio integrations show additional internal structure that is not statistically significant at the 3σ level, and $\gg$20 signal-to-noise

[10] https://telescope.livjm.ac.uk/TelInst/Inst/IOO/
[11] https://telescope.livjm.ac.uk/TelInst/Pipelines/

Table 1
GRB 190114C LT Observations with RINGO3 *BV/R/I*, IO:O *r* Bands, and MASTER VWF/MASTER II Observations in an *r*-equivalent Band

Band	$t_{\rm mid}$ (s)	$t_{\rm exp}/2$ (s)	mag	mag err	F_ν (Jy)	F_ν err (Jy)
BV	202.5	1.2	14.33	0.06	6.64e-03	3.8e-04
BV	204.8	1.2	14.36	0.06	6.49e-03	3.7e-04
BV	207.2	1.2	14.32	0.06	6.70e-03	3.9e-04
BV	209.5	1.2	14.36	0.06	6.49e-03	3.7e-04
BV	211.9	1.2	14.38	0.06	6.37e-03	3.7e-04
BV	...	...	...	...	...	...

Note. Here $t_{\rm mid}$ corresponds to the mean observing time and $t_{\rm exp}$ to the length of the observation window. Magnitudes and flux density values are corrected for atmospheric and Galactic extinction.

(This table is available in its entirety in machine-readable form.)

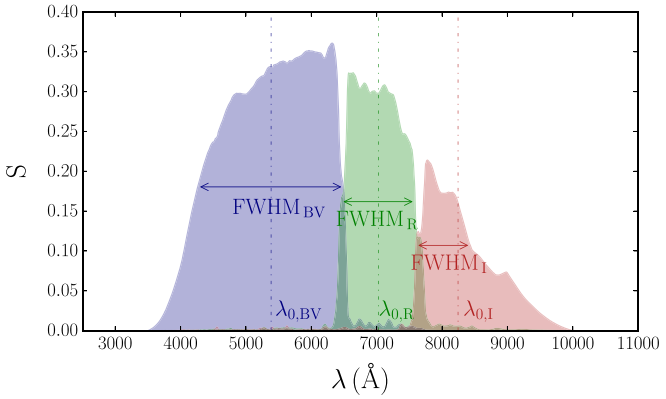

Figure 2. Photonic response functions of the RINGO3 *BV/R/I* bandpasses, which encompass the total instrument throughput (including atmospheric extinction).

ratios further smooth minor features and reject fainter OT detections at later times.

To test for instrument stability during the RINGO3 observations, we study the flux variability of the only star in the field (CD-27 1309; ∼11 mag star). Using the OT binning, CD-27 1309 photometry presents an ∼0.01 mag deviation from the mean in all bands (or ∼1% in flux).

The IO:O observations started 34.7 minutes postburst with the *r* filter. Given that the OT signal-to-noise ratio is ∼40 for each of the 10 s frames, we derive its flux from the six exposures individually. The IO:O *r* magnitudes are standardized using five ∼14–15 mag stars from the Pan-STARRS DR1 catalog (Chambers et al. 2016). In Table 1 and Figure 1, we present the IO:O *r*-filter photometry. The IO:O light curve is corrected for the mean Galactic extinction $A_r = 0.034 \pm 0.001$ mag ($E_{B-V,\rm MW} = 0.0124 \pm 0.0005$ is derived[12] from a $5' \times 5'$ field statistic; Schlegel et al. 1998) but not for host galaxy extinction (see Section 3.3.3).

2.1.2. RINGO3 Bandpass Standardization

After the RINGO3 polaroid, the light is split by two dichroic mirrors into three beams that are simultaneously recorded by three EMCCD cameras (Arnold et al. 2012). In Figure 2, we derive the photonic response function of the RINGO3 instrument, which accounts for atmospheric extinction of the site[13], telescope optics,[14] instrument dichroics,[15] lenses (Arnold 2017), filters,[16,17] transmission, and the quantum efficiency of the EMCCDs (Arnold 2017). The total throughput results in three broad bandpasses with mean photonic wavelengths $\lambda_{0,\{\rm BV,R,I\}} = 5385, 7030, 8245$ Å and FWHMs$_{\{BV,R,I\}} = 2232, 1130, 835$ Å.

Because of the different spectral coverage of RINGO3 bandpasses relative to other photometric systems and the ∼0.02–0.05 mag photometric precision, we standardize RINGO3 magnitudes in the Vega system following Johnson & Morgan's (1953) procedure. Observations of four unreddened A0-type stars (HD 24083, HD 27166, HD 50188, and HD 92573) and the GRB 190114C field were submitted via LT phase2UI[18] using the same instrumental setup as the night of the burst and autonomously dispatched on the nights of 2019 January 30–31. We standardize the magnitudes in the RINGO3 system using the CD-27 1309 star, which adds ∼0.05 mag uncertainty to the photometry.

Taking into account the notation $m = -2.5\ \log(F_\nu) + C_\nu$, with F_ν in erg cm^{-2} s^{-1} Hz^{-1} (e.g., Bessell & Murphy 2012), we compute the magnitude–to–flux density conversion C_ν by deriving the mean flux density F_ν of the Vega star (α Lyr) composite spectrum[19] through each RINGO3 band (Bohlin et al. 2014). We set $m = 0$ for all bandpasses, and we obtain $C_{\nu,\{BV,R,I\}} = -48.60, -48.90, -49.05$.

In Table 1 and Figure 1, we present the GRB 190114C absolute flux-calibrated photometry of the RINGO3 *BV/R/I* bands. All three light curves start at a mean time $T_0 + 202.5$ s. The *R*- and *I*-band photometry ends at ∼7000 s postburst. For the *BV* band, the stacking does not reach the signal-to-noise ratio ⩾20 threshold for the last ∼800 s of observations; therefore, the photometry is discarded. Magnitudes and flux density are corrected for atmospheric extinction with $M_{c,\{BV,R,I\}} = 0.14$, 0.04, 0.02 mag and $F_{c,\{BV,R,I\}} = 0.89, 0.96, 0.98$, respectively, which we compute from a weighted mean of the bandpass throughput and the theoretical atmospheric extinction of the site[13]. We also correct for the mean Galactic extinction, $A_{\{BV,R,I\}}/E_{B-V} = 3.12, 2.19, 1.73$, with $E_{B-V,\rm MW} = 0.0124 \pm 0.0005$ (Schlegel et al. 1998), which we derive using the Pei (1992) Milky Way dust extinction profile. The light curves are not corrected for host galaxy extinction (see Section 3.3.3).

2.1.3. RINGO3 Polarization Calibration

To derive the polarization of a source with RINGO3 instrumental configuration, we first compute the OT flux at each rotor position of the polaroid with aperture photometry using the ASTROPY PHOTUTILS package (Bradley et al. 2016). The flux values are converted to Stokes parameters *q*–*u* following the Clarke & Neumayer (2002) procedure and then to polarization degree and angle. Following Słowikowska et al. 's (2016) methodology to correct for RINGO3 polarization

[12] https://irsa.ipac.caltech.edu/applications/DUST/
[13] https://www.ing.iac.es/Astronomy/observing/manuals/ps/tech_notes/tn031.pdf
[14] https://telescope.livjm.ac.uk/Pubs/LTTechNote1_TelescopeThroughput.pdf
[15] https://telescope.livjm.ac.uk/TelInst/Inst/RINGO3/
[16] https://www.meadowlark.com/versalight-trade-polarizer-p-79?mid=6#.Wun27maZMxE
[17] https://www.thorlabs.com/newgrouppage9.cfm?objectgroup_id=870
[18] https://telescope.livjm.ac.uk/PropInst/Phase2/
[19] We use the alpha_lyr_stis_008.fits spectrum version from the CALSPEC archive.

instrumental effects, we use 44 observations of BD +32 3739, BD +28 4211, and HD 212311 unpolarized stars and 41 observations of HILT 960 and BD +64 106 polarized stars for each band. Due to the positive nature of polarization,[20] measurements are not normally distributed in the low signal-to-noise ratio and low-polarization regime (Simmons & Stewart 1985). Consequently, to derive the confidence levels in the Stokes parameters and polarization, we perform a Monte Carlo error propagation starting with 10^5 simulated flux values for each rotor position.

Following Mundell et al. (2013), we initially infer the polarization of the source with a single measurement with a maximum signal-to-noise ratio. By coadding the 2.34 s frames of the first 10 minute epoch, we obtain a signal-to-noise ratio detection of ∼130 corresponding to a mean time of ∼321 ± 120 s. From this estimate, we derive a polarization degree at the 2σ confidence level of $P_{\{BV,R,I\}} = 2.2^{+0.9}_{-0.8}\%$, $2.9^{+0.9}_{-0.8}\%$, $2.4^{+0.9}_{-0.8}\%$; angle $\theta_{\{BV,R,I\}} = 81° \pm 12°$, $70° \pm 9°$, $71° \pm 11°$; and Stokes parameters $q_{\{BV,R,I\}} = -0.021 \pm 0.006$, -0.022 ± 0.006, -0.019 ± 0.006, and $u_{\{BV,R,I\}} = 0.007 \pm 0.006$, 0.019 ± 0.006, 0.015 ± 0.006. In this paper, we quote a 2σ confidence level for the polarization degree P and angle θ because it better reflects the non-Gaussian behavior of polarization in the low-degree regime.

Polarization is a vector quantity; variation in either or both degree/angle on timescales shorter than $\Delta t \sim 240$ s can result in a polarization detection of lower degree. To check for variability in polarization on timescales $\Delta t < 240$ s, we dynamically coadd the 2.34 s frames at a lower signal-to-noise ratio such that they reach a threshold of ∼70. With this choice, we can claim polarization variability at a 3σ confidence level if we measure a change in the polarization degree of $\gtrsim$3%. Integrations at higher and lower signal-to-noise ratios reproduce the results within 1σ; however, because we estimate polarization to be ∼2%–3%, ≪50 signal-to-noise integrations are dominated by instrumental noise and are essentially upper limits. The remaining frames of the first 10 minute epoch and the following 2 × 10 minutes are coadded as individual measurements to ensure a maximal signal-to-noise ratio. We do not use the next 8 × 10 minute epochs because the signal-to-noise ratio declines below ∼10 and falls within the instrument sensitivity; the instrumental noise is dominating polarization detections of $\lesssim$6%.

In Table 2, we present the Stokes parameters and the polarization degree and angle for the three RINGO3 bandpasses. To check for instrument stability, we calculate the star CD-27 1309 polarization using the OT binning choice. The star CD-27 1309 manifests deviations of ∼0.15% from the mean. Due to the sensitivity of polarization with the photometric aperture employed, we check that apertures within 1.5–3 FWHM yield polarization measurements compatible within 1σ for both CD-27 1309 and the OT.

2.2. Follow-up Observations by the MASTER Global Robotic Net

The earliest detection of GRB 190114C afterglow was done 30.7 s postburst with the VWF camera from the MASTER–SAAO observatory, which is part of the MASTER Global Robotic Net (Lipunov et al. 2010; Kornilov et al. 2012). About 8 s later, the MASTER–IAC VWF also detected the OT. The VWF camera enables wide-field coverage in a white band and constant sky imaging every 5 s, which is crucial for GRB prompt detections (Gorbovskoy et al. 2010).

At ∼47 s postburst, the MASTER–SAAO and MASTER–IAC observatories started nearly synchronized observations with MASTER II. This instrument consists of a pair of 0.4 m twin telescopes with their polaroids fixed at orthogonal angles: MASTER–IAC II at 0°/90° and MASTER–SAAO II at 45°/135°. This configuration allows early-time white-band photometry (see Section 2.2.1) and, when there are two sites simultaneously observing the OT, enables polarization measurements (see Section 2.2.2).

For both the MASTER VWF and MASTER II instruments, we use aperture photometry to derive the source flux (ASTROPY PHOTUTILS; Bradley et al. 2016).

2.2.1. MASTER VWF and MASTER II Light Curves

The MASTER–SAAO VWF and MASTER–IAC VWF cameras started observations at $T_0 + 30.7$ and 38.6 s, respectively; by $\sim T_0 + 50$ s, the OT signal-to-noise ratio falls under 5, and the photometry is discarded. We standardize the VWF white band with the r band using five stars of 8–10 mag from the Pan-STARRS DR1 catalog (Chambers et al. 2016).

MASTER–SAAO II and MASTER–IAC II observed the OT since 45.9 and 48 s postburst, respectively. Given this instrumental setup, we align and average the field frames from the two orthogonal polaroid positions and derive a single photometric measurement per site. Additionally, we apply the RINGO3 photometric criterion, and we only accept OT detections with signal-to-noise ratios over 20 (see Section 2.1.1). We standardize the MASTER II white band to the r band using five stars of 13–15 mag from the Pan-STARRS DR1 catalog. During MASTER II observations, these stars present an ∼0.04 mag deviation from the mean. Both MASTER VWF and MASTER II photometry are corrected for mean Galactic extinction $A_r = 0.034 \pm 0.001$ mag (Schlegel et al. 1998) and presented in Table 1 and Figure 1.

2.2.2. MASTER II Polarization Calibration

There have been several lower-bound polarization measurements with only one MASTER II site (Gorbovskoy et al. 2016; Troja et al. 2017). For GRB 190114C, MASTER–SAAO II and MASTER–IAC II responded to the BAT trigger almost simultaneously—since ∼47 s postburst and with an initial temporal lag of ∼2.2 s—allowing us to completely sample the Stokes plane and measure the polarization degree and angle.

To derive the polarization, we first subtract the relative photometric zero-point between the MASTER–SAAO and MASTER–IAC observations using field stars. Due to the temporal lag between the two telescopes sites and the fading nature of the source, we also correct for the relative intensity by interpolating over the two time windows. Following the RINGO3 calibration, we use the Clarke & Neumayer (2002) method to derive the Stokes q–u parameters, the polarization degree/angle, and the confidence levels (see Section 2.1.3). We use RINGO3 polarization measurements of the CD-27 1309 star ($P = 0.1\%$–0.3%) to subtract MASTER II instrumental polarization ($P \sim 7\%$); by doing this, the polarization

[20] The polarization degree and angle are related to the Stokes parameters as $p = \sqrt{q^2 + u^2}$ and $\theta = 0.5 \arctan(u/q)$.

Table 2
GRB 190114C Polarization Observations with LT RINGO3 *BV/R/I* Bands and MASTER II White Band

Band	t_{mid} (s)	$t_{exp}/2$ (s)	S/N	q	q_{err}	u	u_{err}	P (%)	P_{err} (%)	θ (deg)	θ_{err} (deg)
BV	223.5	22.1	71	−0.020	0.022	0.018	0.011	2.7	$^{+1.7}_{-1.4}$	69	$^{+18}_{-18}$
BV	283.3	39.7	70	−0.019	0.022	0.009	0.011	2.1	$^{+1.7}_{-1.3}$	77	$^{+25}_{-25}$
BV	433.4	112.4	70	−0.020	0.022	0.019	0.011	2.8	$^{+1.7}_{-1.4}$	68	$^{+17}_{-17}$
BV	671.5	127.7	50	−0.027	0.031	0.023	0.016	3.6	$^{+2.4}_{-2.0}$	70	$^{+19}_{-19}$
BV	1117.2	298.9	54	−0.022	0.029	0.027	0.014	3.5	$^{+2.1}_{-1.8}$	64	$^{+18}_{-18}$
BV	1734.1	298.9	38	−0.027	0.041	0.036	0.020	4.5	$^{+3.0}_{-2.5}$	63	$^{+20}_{-20}$
R	215.3	13.9	70	−0.025	0.022	0.029	0.011	3.8	$^{+1.7}_{-1.5}$	65	$^{+12}_{-12}$
R	245.8	18.6	71	−0.029	0.022	0.010	0.011	3.0	$^{+1.6}_{-1.4}$	80	$^{+16}_{-16}$
R	293.8	31.5	70	−0.028	0.022	0.023	0.011	3.6	$^{+1.6}_{-1.5}$	70	$^{+13}_{-13}$
R	386.5	63.2	70	−0.019	0.022	0.014	0.011	2.4	$^{+1.7}_{-1.4}$	71	$^{+21}_{-21}$
R	623.4	175.8	61	−0.024	0.026	0.007	0.013	2.5	$^{+1.9}_{-1.5}$	82	$^{+23}_{-24}$
R	1117.2	298.9	45	−0.029	0.035	0.008	0.017	3.0	$^{+2.6}_{-2.0}$	83	$^{+27}_{-27}$
R	1734.1	298.9	31	−0.006	0.051	0.020	0.026	2.1	$^{+4.0}_{-1.6}$	53	$^{+110}_{-43}$
I	215.2	13.9	70	−0.036	0.022	0.023	0.011	4.2	$^{+1.6}_{-1.5}$	74	$^{+11}_{-11}$
I	245.7	18.6	70	−0.018	0.022	0.003	0.011	1.8	$^{+1.7}_{-1.2}$	86	$^{+29}_{-29}$
I	292.6	30.3	70	−0.022	0.022	0.020	0.011	3.0	$^{+1.7}_{-1.4}$	69	$^{+16}_{-16}$
I	380.6	59.7	70	−0.012	0.022	0.012	0.011	1.7	$^{+1.7}_{-1.2}$	67	$^{+34}_{-32}$
I	618.7	180.5	63	−0.024	0.025	0.007	0.012	2.5	$^{+1.9}_{-1.5}$	82	$^{+22}_{-22}$
I	1117.2	298.9	45	−0.007	0.035	0.003	0.017	0.8	$^{+2.9}_{-0.5}$	78	$^{+92}_{-69}$
I	1734.1	298.9	33	0.019	0.048	−0.025	0.024	3.2	$^{+3.7}_{-2.3}$	154	$^{+23}_{-148}$
White	52.0	6.1	264	-0.076	0.005	-0.015	0.005	7.7	$^{+1.1}_{-1.1}$	96[a]	$^{+4}_{-4}$
White	78.4	5.0	147	…	…	…	…	>2.2	$^{+0.6}_{-0.6}$	…	…
White	108.6	8.8	135	-0.020	0.012	0.003	0.012	2.0	$^{+2.6}_{-1.5}$	85[a]	$^{+44}_{-43}$
White	149.6	12.3	103	0.012	0.014	0.002	0.014	1.2	$^{+3.1}_{-0.8}$	4[a]	$^{+175}_{-2}$
White	200.7	16.0	78	0.021	0.019	0.003	0.019	2.1	$^{+4.3}_{-1.5}$	4[a]	$^{+174}_{-3}$

Note. Here t_{mid} corresponds to the mean observing time, t_{exp} to the length of the observation window, and S/N to the signal-to-noise ratio of the OT. The Stokes parameters q–u, the polarization degree P, and the polarization angle θ are corrected for instrumental effects. The P and θ uncertainties are quoted at a 2σ confidence level.
[a] Here θ is not calibrated with polarimetric standard stars.

contribution from the interstellar medium is also removed. During MASTER II observations, the CD-27 1309 star shows deviations of ∼0.3% from the mean.

Although the burst is bright at that time, the signal-to-noise ratio and polarization degree rapidly drop within the first ∼100 s; we discard observations after $\sim T_0 + 200$ s. Additionally, we derive a lower bound of the polarization degree at $\sim T_0 + 73$ s—because the 0°/90° MASTER–IAC II frames were not taken—using $P_{low} = (I_2 - I_1)/(I_1 + I_2)$, where I_1 and I_2 are the source intensity at each orthogonal polaroid position (see Gorbovskoy et al. 2016 and Troja et al. 2017 for the procedure). In Table 2, we present the Stokes parameters and polarization degree and angle for the MASTER II observations. We note that the angle is not calibrated with polarimetric standard stars, which implies that we cannot determine its evolution from MASTER II to RINGO3 observations.

3. Results

Here we present the temporal properties of the optical emission (Section 3.1), optical polarization (Section 3.2), and spectral analysis of the optical and X-ray emission (Section 3.3).

3.1. The Emission Decay of the Early Optical Afterglow

A simple power-law model yields a poor fit to the RINGO3 light curves (see Table 3). Consequently, we attempt a broken power-law fit to each band, which significantly improves the χ^2 statistics (see Table 3 and Figure 3). This result indicates a light-curve flattening from $\alpha_{opt} \sim 1.5$ to 1 at $t_{break,\{BV,R,I\}} = 401 \pm 10$, 443^{+11}_{-7}, 525^{+11}_{-12} s postburst. There is a discrepancy between the break times of the three bands that cannot be reconciled within 3σ, indicating that the break is chromatic and moving redward through the bands.

A broken power-law model also gives a good fit to the *r*-equivalent MASTER VWF, MASTER II, and IO:O joint light curve (see Table 3 and Figure 3). Early-time observations from the MASTER VWF prove that the optical emission had already been decaying as a simple power law since 30.7 s postburst with $\alpha_{opt} = 1.669 \pm 0.013$. At $T_0 + 407^{+20}_{-19}$ s, consistent with the RINGO3 *BV* break time, the light curve flattens to $\alpha_{opt} = 1.054 \pm 0.011$.

3.2. Time-resolved Polarimetry in White and Three Optical Bands

During the first ∼50 s of MASTER II observations, the polarization degree displays an early-time drop from 7.7% ±

Table 3
Results of the Models Applied to GRB 190114C Light Curves for LT RINGO3 *BV/R/I*, MASTER VWF/MASTER II *r*-equivalent, and LT IO:O *r* Optical Bands

Band	Instrument	α_1	α_2	t (s)	Model	χ^2/dof	p-value	Figure
BV	RINGO3	1.082 ± 0.007	⋯	⋯	PL[a]	627/332	<0.0001	⋯
BV	RINGO3	1.49 ± 0.02	1.005 ± 0.006	401 ± 10	BPL[b]	290/331	0.95	3
r	MASTER + IO:O	1.33 ± 0.02	⋯	⋯	PL	745/43	<0.0001	3
r	MASTER + IO:O	1.669 ± 0.013	1.054 ± 0.011	407^{+20}_{-19}	BPL	36/42	0.72	3
R	RINGO3	1.147 ± 0.006	⋯	⋯	PL	1432/389	<0.0001	⋯
R	RINGO3	1.575 ± 0.013	1.040 ± 0.004	443^{+11}_{-7}	BPL	345/388	0.94	3
I	RINGO3	1.110 ± 0.008	⋯	⋯	PL	2179/365	<0.0001	⋯
I	RINGO3	1.546 ± 0.011	0.962 ± 0.005	525^{+11}_{-12}	BPL	369/364	0.41	3
BV,r,R,I	MASTER + RINGO3 + IO:O	2.35 ± 0.05	0.905 ± 0.009	⋯	2 PLs	1406/1127	<0.0001	9
BV,r,R,I	MASTER + RINGO3 + IO:O	1.711 ± 0.012	0.707 ± 0.010	805 ± 19, 831 ± 47, 931 ± 18, 1083 ± 20	PL + BPL	1174/1123	0.14	9

Notes. The first part of Table 3 includes all of the phenomenological models, and the second part includes the two physical models that relate to a "reverse-plus-forward shock" scenario.
[a] PL: power law.
[b] BPL: broken power law.

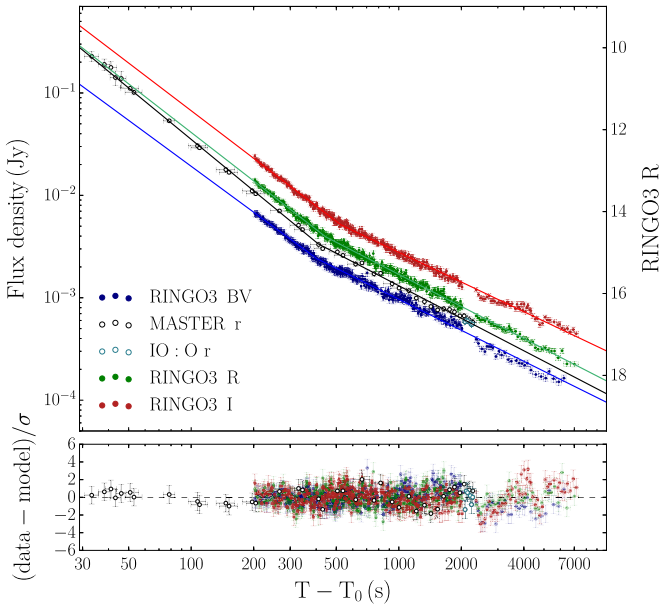

Figure 3. The GRB 190114C LT and MASTER light curves modeled in terms of broken power laws: RINGO3 *BV/R/I* bands and the joint *r*-equivalent MASTER VWF/MASTER II/IO:O band. The results of the fits are listed in Table 3. The bottom panel corresponds to the residuals of the fit. In the *x*-axis, T_0 corresponds to BAT trigger time; in the *y*-axis, the flux density is converted to RINGO3 *R* magnitude.

1.1% to $2.0^{+2.6}_{-1.5}$%, consistent with the constant low polarization degree measured by RINGO3 from ∼200 s onward (see Figure 4). From 52 to 109 s postburst, the polarization angle remains constant within the uncertainties (see Table 2).

RINGO3 time-resolved polarization shows a constant degree and angle within a 2σ confidence level during ∼200–2000 s postburst (see Figure 5), ruling out any temporal trend at these timescales or swings in polarization bigger than $\Delta P \sim 3\%$ for $t \sim$ 200–450 s postburst and at a 3σ confidence level. The temporal behavior of polarization agrees with the value inferred in Section 2.1.3 from the maximum signal-to-noise ratio integration $P_{\{BV,R,I\}} = 2.2^{+0.9}_{-0.8}\%$, $2.9^{+0.9}_{-0.8}\%$, $2.4^{+0.9}_{-0.8}\%$ and $\theta_{\{BV,R,I\}} = 81° \pm 12°$, $70° \pm 9°$, $71° \pm 11°$ (see Figure 5; black lines) and the median value $P_{\{BV,R,I\}} = 3.1\% \pm 0.4\%$, $3.0\% \pm 0.6\%$, $2.5\% \pm 0.7\%$ and $\theta_{\{BV,R,I\}} = 68° \pm 3°$, $71° \pm 9°$, and $78° \pm 7°$ (quoting the median absolute deviation; see Figure 5, dotted lines). The behavior is the same in all three bands.

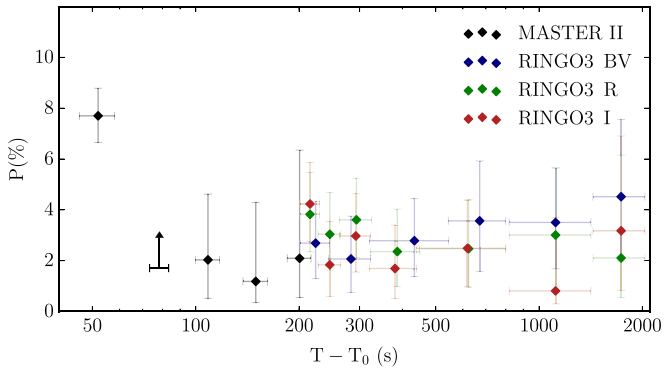

Figure 4. MASTER II and RINGO3 temporal evolution of the polarization degree. Uncertainties are quoted at a 2σ confidence level. The black arrow corresponds to a 2σ lower bound of the polarization degree.

3.3. The Spectral Evolution of the Afterglow

To spectrally characterize GRB 190114C during RINGO3 observations, we test for color evolution in the optical (Section 3.3.1), we study the spectral evolution of the 0.3–150 keV X-ray band for the time intervals of Figure 6 (Section 3.3.2), and we check how the optical and X-ray connect (Section 3.3.3).

3.3.1. Color Evolution through RINGO3 Bands

Taking advantage of the simultaneity of RINGO3 three-band imaging, we attempt to infer the evolution of the optical spectral index. To guarantee a spectral precision of ∼0.05–0.06 mag per measurement, we take the lowest signal-to-noise ratio light curve (*BV* band) and we dynamically coadd frames so the OT reaches a signal-to-noise ratio threshold of ⩾40. Following that, we coadd *R/I* frames using the *BV*-band

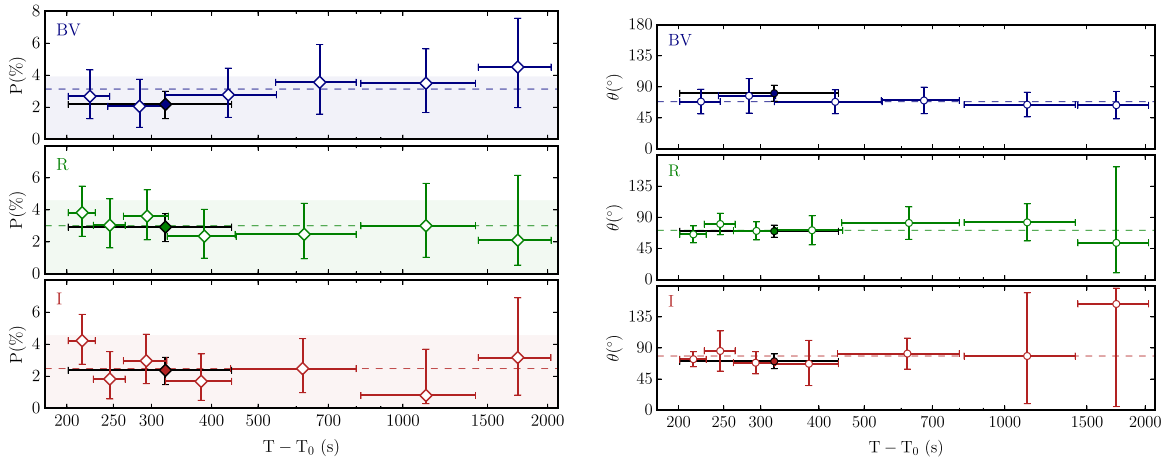

Figure 5. The GRB 190114C temporal evolution of the polarization degree (left) and angle (right) for the three RINGO3 bands. In black, we show the maximum signal-to-noise ratio integration. Uncertainties are quoted at a 2σ confidence level. Dotted lines correspond to the median value, and the shaded regions correspond to the maximum polarization degree induced by dust in the line of sight, including the highly extincted host galaxy and a small contribution from the Milky Way ($E_{B-V,\mathrm{HG}} = 0.51 \pm 0.04$; $E_{B-V,\mathrm{MW}} = 0.0124 \pm 0.0005$). Here T_0 corresponds to BAT trigger time.

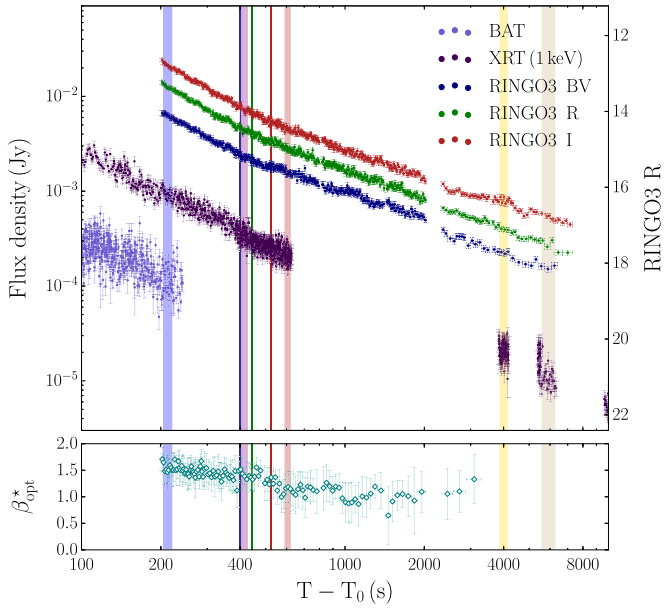

Figure 6. The GRB 190114C BAT/XRT (Evans et al. 2009) and RINGO3 *BV/R/I* light curves with the observations used for the broadband SED modeling highlighted in shaded colors. The vertical solid lines are RINGO3 *BV/R/I* light-curve break times. The bottom panel corresponds to the optical spectral index inferred from the RINGO3 *BV/R/I* bands without considering host galaxy extinction. In the *x*-axis, T_0 corresponds to BAT trigger time; in the *y*-axis, the flux density is converted to RINGO3 *R* magnitude.

binning, and for every three-band spectral energy distribution (SED), we fit a power law.

In Figure 6, we present the evolution of the optical spectral index $\beta^{\star}_{\mathrm{opt}}$; this index is not corrected for host galaxy extinction (see Section 3.3.3), which makes this measurement an upper limit of the intrinsic β_{opt}. Spectral indexes exhibit a decreasing behavior from $\beta^{\star}_{\mathrm{opt}} \sim 1.5$ to 1 masked by the uncertainties. Due to the number of measurements available, we perform a Wald–Wolfowitz runs test (Wald & Wolfowitz 1940) of all the points against the median value to check for a trend. If there is no real decrease of the spectral index, the data should fluctuate randomly around the median. In this case, a run is a consecutive series of $\beta^{\star}_{\mathrm{opt}}$ terms over or under the median. The temporal evolution of the spectral indexes displays significantly smaller number of runs than expected with a *p*-value $= 2 \times 10^{-15}$, which rejects the hypothesis of randomness and indicates that a temporal trend from soft to harder spectral indexes is likely. This result is in agreement with the chromatic nature of the break observed in the RINGO3 light curves.

3.3.2. The 0.3–150 keV X-Ray Spectra

For the X-ray spectral analysis, we use the available BAT-XRT observations that correspond to the time intervals of Figure 6. With this choice, the first spectrum is before the slope change of the optical light curve at ∼400–500 s postburst (see Section 3.1). Due to the synchrotron nature of the afterglow, the models used for this analysis comprise either a single power law or connected power laws.

We extract the time-resolved 0.3–10 keV XRT spectra using the web interface provided by Leicester University[21] based on HEASOFT (v6.22.1; Blackburn 1995). Energy channels are grouped with the GRPPHA tool so that we have at least 20 counts bin^{-1} to ensure the Gaussian limit and adopt χ^2 statistics. The first four time intervals were observed in WT mode and the final one in PC mode. For modeling WT observations, we only consider energies $\geqslant 0.8$ keV due to an instrumental effect that was reported in Beardmore (2019). Simultaneous time-resolved, 15–150 keV spectra with BAT are extracted for the first three time intervals using the standard BAT pipeline (e.g., see Rizzuto et al. 2007) and are finally grouped in energy to ensure a $>2\sigma$ significance.

The combined BAT-XRT spectra are modeled under XSPEC (v. 12.9.1; Arnaud et al. 1999) using χ^2 statistics with a simple absorbed power law (POWERLAW*PHABS*ZPHABS) that accounts for the rest-frame host galaxy total hydrogen absorption, $N_{\mathrm{H,HG}}$, and the Galactic[22] $N_{\mathrm{H,MW}} = 7.54 \times 10^{19}\,\mathrm{cm}^{-2}$ (Willingale et al. 2013). By satisfactorily fitting each spectrum with a power law, we find that the 0.3–10 keV and 15–150 keV spectra belong to the same spectral regime and that there is no significant spectral evolution during the first ∼200–6000 s postburst. In Figure 7, we fit all five spectra with a single

[21] http://www.swift.ac.uk/user_objects/

[22] Derived using the https://www.swift.ac.uk/analysis/nhtot/ tool.

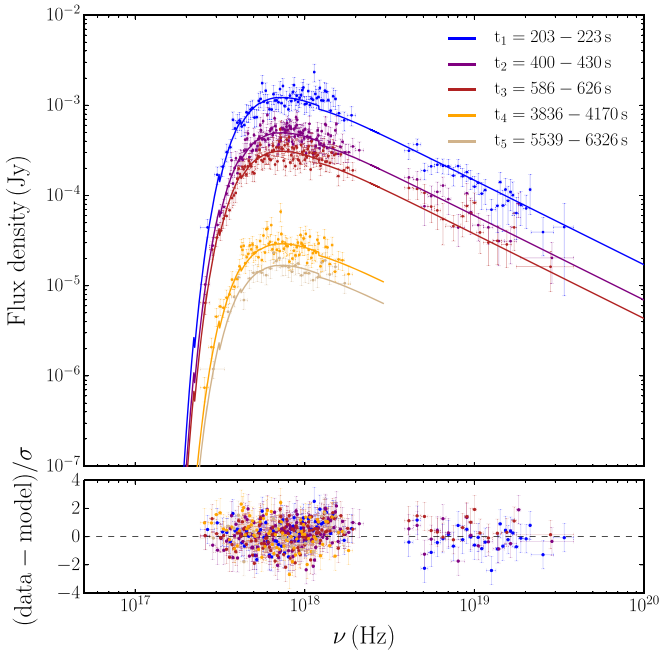

Figure 7. The GRB 190114C X-ray spectra of the combined 0.3–10 keV XRT and 15–150 keV BAT observations (Evans et al. 2009). The spectra are modeled with an absorbed power law that accounts for the Galactic and host galaxy rest-frame total hydrogen absorption. The results of the fit are $\beta_x = 0.94 \pm 0.02$, $N_{H,HG} = (9.3 \pm 0.2) \times 10^{22}$ cm^{-2}, $\chi^2/\mathrm{dof} = 422/466$, and p-value $= 0.89$. The bottom panel corresponds to the residuals of the fit.

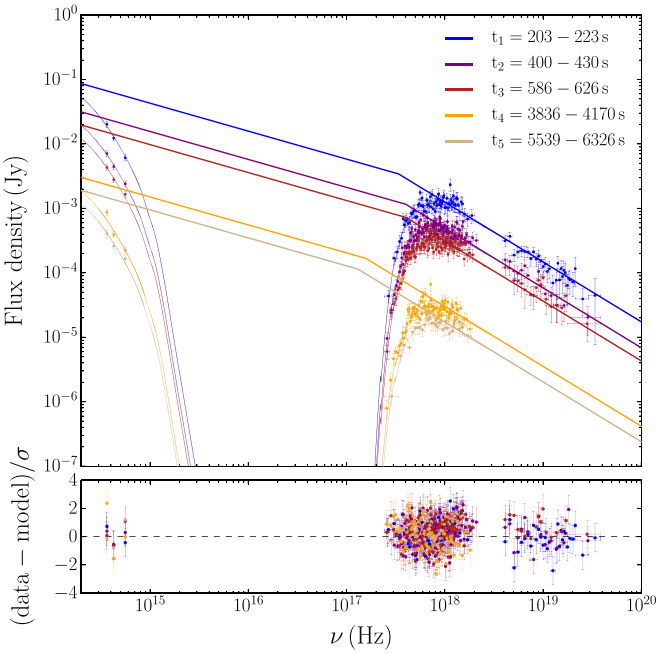

Figure 8. The GRB 190114C broadband SEDs with RINGO3, XRT, and BAT observations (Evans et al. 2009). The SEDs are best fitted with a broken power-law model that accounts for extinction in the optical and total hydrogen absorption in the X-ray. The results of the fit are $\beta_{opt} = 0.43 \pm 0.02$; $\beta_x = 0.93 \pm 0.02$; $E_{break,\{1,2,3,4,5\}} = 1.4 \pm 0.3$, 1.6 ± 0.2, 1.6 ± 0.3, 0.65 ± 0.14, 0.54 ± 0.12 keV; $\chi^2/\mathrm{dof} = 439/481$; and p-value $= 0.82$. In the host galaxy rest frame, $A_{v,HG} = 1.49 \pm 0.12$ mag and $N_{H,HG} = (9.0 \pm 0.3) \times 10^{22}$ cm^{-2}. The bottom panel corresponds to the residuals of the fit.

spectral index. The fit procedure results in a spectral index $\beta_x = 0.94 \pm 0.02$, rest-frame hydrogen absorption $N_{H,HG} = (9.3 \pm 0.2) \times 10^{22}$ cm^{-2}, $\chi^2/\mathrm{dof} = 422/466$, and p-value $= 0.89$. Due to the high column density absorption among the soft X-rays, the slope is mainly constrained by the hard X-rays.

3.3.3. Broadband SEDs

We obtain the combined BAT-XRT-RINGO3 SEDs by coadding those RINGO3 frames that correspond to a given X-ray epoch and then deriving the absolute flux-calibrated photometry (see Section 2.1.2).

Broadband SEDs are also modeled under XSPEC using χ^2 statistics with a simple absorbed power law (POWERLAW*ZDUST*ZDUST*PHABS*ZPHABS) that accounts for total hydrogen absorption (see Section 3.3.2), Galactic extinction ($E_{B-V,MW} = 0.0124 \pm 0.0005$; Schlegel et al. 1998), and a rest-frame Small Magellanic Cloud (SMC) dust extinction profile for the host galaxy (Pei 1992).

The optical and X-ray fluxes do not connect with a simple absorbed power law. Consequently, we test for a break between the two spectral regimes (using the BKNPOWER model). For all five SEDs, we link all parameters relating to absorption, extinction, and spectral indexes, and we leave the break frequency as a free parameter for each SED. From the broken power-law fit (see Figure 8), we obtain a spectral index $\beta_{opt} = 0.43 \pm 0.02$ for the optical and $\beta_x = 0.93 \pm 0.02$ for the X-ray with $\chi^2/\mathrm{dof} = 439/481$ and p-value $= 0.82$. The break evolves as $E_{break,\{1,2,3,4,5\}} = 1.4 \pm 0.3$, 1.6 ± 0.2 , 1.6 ± 0.3, 0.65 ± 0.14, 0.54 ± 0.12 keV. We derive high-extinction $A_{v,HG} = 1.49 \pm 0.12$ mag or, equivalently, $E_{B-V,HG} = 0.51 \pm 0.04$ and absorption $N_{H,HG} = (9.0 \pm 0.3) \times 10^{22}$ cm^{-2} at the host galaxy rest frame. We achieve compatible results within 1σ for spectral indexes, energy breaks, and total hydrogen absorption using Large Magellanic Cloud/Milky Way dust extinction profiles, which gives $A_{v,HG} = 1.64 \pm 0.13$ and 1.72 ± 0.12 mag, respectively.

4. Theoretical Modeling

4.1. Modeling the Optical Afterglow

In the standard fireball model, possible mechanisms that produce chromatic breaks include the passage of a break frequency through the band, a change in the ambient density profile, or an additional emission component (Melandri et al. 2008). We rule out that the light-curve flattening at ∼400–500 s postburst and magnitude ∼14 is due to an emerging supernova —Melandri et al. (2019) reported a supernova component 15 days postburst—or host galaxy contamination. Additionally, optical emission from ongoing central engine activity is unlikely: BAT/XRT emission is already decaying since ∼30 and ∼70 s postburst, respectively (see Figure 1).

Several GRBs exhibit a similar light-curve flattening from $\alpha_{opt,1} \sim 1.3$–1.7 to $\alpha_{opt,2} \sim 0.8$–1.1 in the optical at early times; see Table 4: GRB 021211 (Fox et al. 2003), GRB 050525A (Shao & Dai 2005), GRB 050904 (Haislip et al. 2006; Wei et al. 2006), GRB 060908 (Covino et al. 2010), GRB 061126 (Gomboc et al. 2008; Perley et al. 2008), GRB 090102 (Steele et al. 2009; Gendre et al. 2010), GRB 090424 (Jin et al. 2013), and GRB 090902B (Pandey et al. 2010). Additionally, most of them bear similar spectral and temporal properties to GRB 190114C in both the optical and X-ray regimes.

For GRB 021211, GRB 050525A, GRB 061126, GRB 090424, and GRB 090902B, the optical excess at the beginning

Table 4
Optical and X-Ray Temporal α and Spectral β Indexes of GRBs with Optical Light Curves that Show a Steep-to-flat Behavior and Decay Rates Comparable to GRB 190114C

GRB	$\alpha_{\rm opt,1}$	$\alpha_{\rm opt,2}$	$\alpha_{\rm x}$	$\beta_{\rm opt}$	$\beta_{\rm x}$	Reference
021211	$\sim$1.6	$\sim$1.1	⋯	$\leqslant$0.98	⋯	Fox et al. (2003)
050525A	$\sim$1.3	$\sim$1	$0.68^{+0.06}_{-2.18}$ − 1.54 ± 0.06	⋯	$0.97^{+0.16}_{-0.15}$	Shao & Dai (2005); Evans et al. (2009)
050904	$1.36^{+0.07}_{-0.06}$	$0.82^{+0.21}_{-0.08}$	$2.02^{+0.06}_{-0.05}$ − $1.39^{+0.06}_{-0.05}$	$\leqslant -1.25^{+0.15}_{-0.14}$	$0.84^{+0.06}_{-0.05}$	Haislip et al. (2006); Evans et al. (2009)
060908	1.5 ± 0.3	1.05 ± 0.03	$1.14^{+0.03}_{-0.02}$	$\sim$0.3	1.1 ± 0.2	Evans et al. (2009); Covino et al. (2010)
061126	1.48 ± 0.06	0.88 ± 0.03	1.290 ± 0.008	0.38 ± 0.03[a]	0.88 ± 0.03	Gomboc et al. (2008)
090102	1.50 ± 0.06	0.97 ± 0.03	1.34 ± 0.02	$\leqslant$1.32	0.83 ± 0.09	Gendre et al. (2010)
090424	$\sim$1.5	$\sim$0.85	0.87 ± 0.02 − 1.17 ± 0.01	⋯	0.87 ± 0.09	Evans et al. (2009); Jin et al. (2013)
090902B	$\sim$1.6	0.90 ± 0.08	1.30 ± 0.04	0.68 ± 0.11	0.9 ± 0.1	Pandey et al. (2010)
190114C	1.669 ± 0.013	$\sim$1	1.345 ± 0.004	0.43 ± 0.02	0.93 ± 0.02	This work

Note.
[a] Here $\beta_{\rm x}$ is linked to $\beta_{\rm opt}$ as $\beta_{\rm x} = \beta_{\rm opt} + 0.5$.

of the light curve favored the presence of reverse shock emission (Fox et al. 2003; Shao & Dai 2005; Gomboc et al. 2008; Perley et al. 2008; Pandey et al. 2010; Jin et al. 2013). Due to a quasi-simultaneous X-ray and optical flare, the GRB 050904 light curve was better understood in terms of late-time internal shocks (Wei et al. 2006). For GRB 090102, Gendre et al. (2010) also considered the possibility of a termination shock caused by a change in the surrounding medium density profile. However, Steele et al.'s (2009) 10% ± 1% polarization measurement during the steep decay of the afterglow favored the presence of large-scale magnetic fields and, therefore, a reverse shock component. Additionally, Mundell et al. (2013) reported a 28% ± 4% polarization degree at the peak of the GRB 120308A optical emission, a decline to 16^{+5}_{-4}%, and a light-curve flattening that was interpreted as a reverse–forward shock interplay. Therefore, we attempt to model GRB 190114C optical emission with a reverse-plus-forward shock model.

4.1.1. Reverse–Forward Shock Model

Under the fireball model framework, the evolution of the spectral and temporal properties of the afterglow satisfies closure relations (Sari et al. 1998; Zhang & Mészáros 2004; Zhang et al. 2006; Racusin et al. 2009; Gao et al. 2013). These depend on the electron spectral index p, density profile of the surrounding medium (interstellar medium (ISM) or wind), cooling regime (slow or fast), and jet geometry. In the reverse shock scenario, the total light-curve flux can be explained by a two-component model that combines the contribution of the reverse and forward shock emission (Kobayashi 2000; Kobayashi & Zhang 2003a; Zhang et al. 2003).

When the fireball starts to decelerate at $t_{\rm peak,r}$, the reverse shock emission produces a bright optical peak; for GRB 190114C, this happened prior to the MASTER/RINGO3 observations. For an ISM profile, slow cooling regime and with the optical band in between the typical synchrotron and cooling frequency, $\nu_{\rm m,r} < \nu_{\rm opt} < \nu_{\rm c,r}$, the emission should decay[23] with $\alpha_{\rm r} = (3p + 1)/4 \sim 2$ for a typical $p \sim 2.3$. Later on, the forward shock peaks when the typical synchrotron frequency $\nu_{\rm m,f}$ crosses the optical band. In the $\nu_{\rm m,f} < \nu_{\rm opt} < \nu_{\rm c,f}$ spectral regime, the forward shock emission will follow an expected decay with $\alpha_{\rm f} = 3(p - 1)/4 \sim 1$, which flattens the light curve. Consequently, the reverse–forward shock model consists of a power law with a temporal decay $\alpha_{\rm r}$ for the reverse shock component plus a forward shock contribution that has an expected rise of 0.5 and decay of $\alpha_{\rm f}$. The GRB 190114C light curves suggest that the forward shock peak time $t_{\rm peak,f}$ happens before or during MASTER/RINGO3 observations and it is masked by the bright reverse shock emission.

In the left panel of Figure 9, we attempt the simplest model by considering that the forward shock peaks before the MASTER observations ($t_{\rm peak,r}$, $t_{\rm peak,f} \ll 30$ s). We leave the reverse and forward shock electron indexes as free parameters. The light curve is best modeled with two power-law components that decay as $\alpha_{\rm opt,r} = 2.35 \pm 0.05$ and $\alpha_{\rm opt,f} = 0.905 \pm 0.009$ (see Table 3). However, the MASTER residuals present a trend, and the model underestimates by $\sim$0.8 mag the late-time observations in the r band reported in the GCN circulars. A decay of $\sim$0.7–0.8 was reported by Kumar et al. (2019b) and Singh et al. (2019) hours to days postburst, which is inconsistent with the $\alpha_{\rm opt,f}$ derived. In addition, UVOT white-band emission was also decaying as $\alpha = 1.62 \pm 0.04$ since $\sim$70 s postburst with a change to $\alpha = 0.84 \pm 0.02$ at $\sim$400 s (Ajello et al. 2020).

In the right panel of Figure 9, we consider a model in which the forward shock peaks during MASTER/RINGO3 observations. In this model, the two emission components decay as $\alpha_{\rm opt,r} = 1.711 \pm 0.012$ and $\alpha_{\rm opt,f} = 0.707 \pm 0.010$, and the forward shock peaks at $t_{\rm peak,f,\{BV,r,R,I\}} = 805 \pm 19, 831 \pm 47, 931 \pm 18, 1083 \pm 20$ s (see Table 3). Both reverse and forward shock decay indexes are compatible with an electron index $p \sim 1.95$. Allowing different peak times for each band is preferred over a fixed peak time model, consistent with a chromatic emergence of the forward shock that moves redward through the bands. The typical synchrotron break frequency is expected to evolve through RINGO3 bands like $\nu_{\rm m,f} \propto t^{-\alpha_{\rm m}}$ with $\alpha_{\rm m} = 1.5$; we find $\alpha_{\rm m} \sim 1.4$.

Even though both models are compatible with the spectral evolution of the optical index $\beta^{\star}_{\rm opt}$ (see Figure 10), the model with the forward shock peak during MASTER/RINGO3 observations is preferred by early- and late-time observations over an early-time forward shock peak (see Table 3 and Figure 9). Photoionization of dust could also cause similar color evolution—with a red-to-blue shift—during the very early stages of the GRB and mainly during the prompt phase (e.g., Perna et al. 2003; Morgan et al. 2014; Li et al. 2018). However, the GRB 190114C blue-to-red color change favors

[23] The decay rate is much slower or faster if the observations are in another spectral regime and/or the emission is due to high-latitude emission (Kobayashi 2000; Kobayashi & Zhang 2003b).

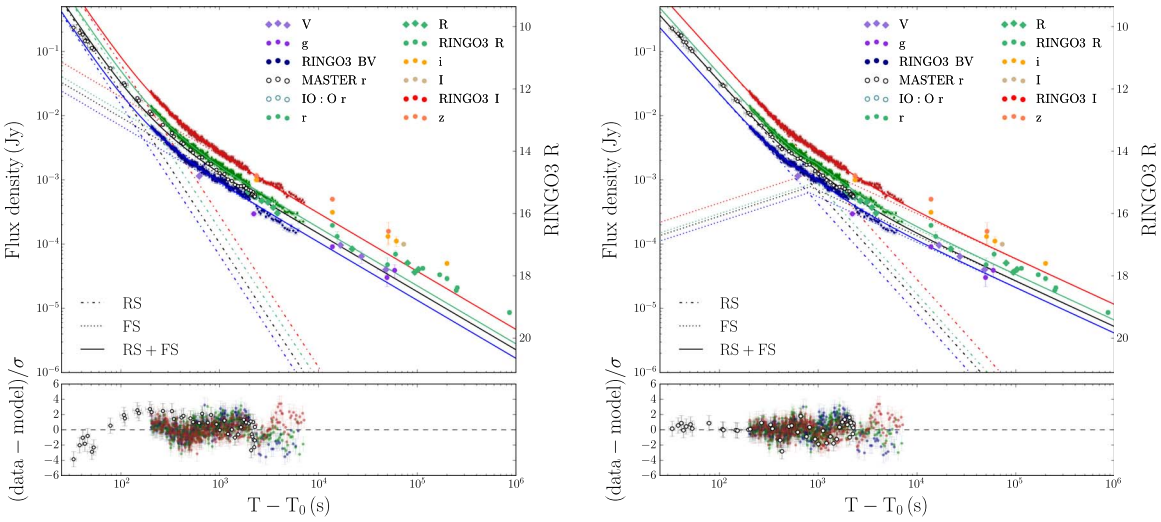

Figure 9. The GRB 190114C MASTER/IO:O *r*-equivalent and RINGO3 *BV/RI* multiwavelength light curves modeled in terms of reverse (RS) plus forward (FS) shock emission. On the left, we model the two components in terms of power laws. On the right, we model the reverse shock with a power law and the forward shock with a broken power law that has fixed $\alpha_1 = 0.5$. The results of both fits are listed in Table 3. The bottom panels correspond to the residuals of the fits. We also display the data reported in GCNs that cover energy ranges similar to RINGO3 bandpasses: UVOT (Siegel & Gropp 2019), NOT (Selsing et al. 2019), OASDG (Izzo et al. 2019), GROND (Bolmer & Schady 2019), REM (D'Avanzo 2019), McDonald Observatory (Im et al. 2019a), LSGT (Kim & Im 2019), GRowth-India (Kumar et al. 2019b), KMTNet (Kim et al. 2019), UKIRT (Im et al. 2019b), CHILESCOPE (Mazaeva et al. 2019a, 2019b, 2019c), RTT150 (Bikmaev et al. 2019), ePESSTO NTT (Ragosta et al. 2019), RATIR (Watson et al. 2019), and HCT (Kumar et al. 2019a; Singh et al. 2019). The GCN observations do not include filter corrections. In the *x*-axis, T_0 corresponds to BAT trigger time; in the *y*-axis, the flux density is converted to RINGO3 *R* magnitude.

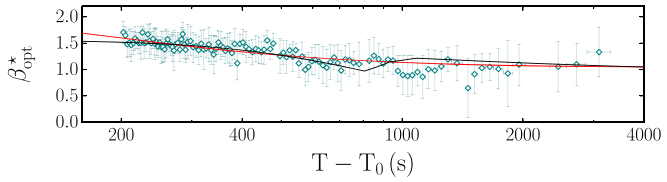

Figure 10. Evolution of the GRB 190114C optical spectral index (not corrected for host galaxy extinction) with the reverse–forward shock models used to fit the optical light curves. Red shows the forward shock model that peaks before observations; black shows the forward shock model that peaks during observations. Here T_0 corresponds to BAT trigger time.

the interpretation of the passage of an additional spectral component through the optical band: the transition from reverse shock–dominated outflow to forward shock emission (e.g., see GRB 061126, Perley et al. 2008; GRB 080319, Racusin et al. 2008; and GRB 130427A, Vestrand et al. 2014). From Table 4, GRB 061126 is also identified among the 70 GRBs of Li et al. 's (2018) classification of color trends as a reverse-to-forward shock transition. Additionally, the reverse–forward shock scenario is supported by radio data (Laskar et al. 2019b).

4.2. The Standard Model for a Normal Spherical Decay

4.2.1. Evidence of a Jet Break in the X-Ray?

After the main γ-ray prompt bulk emission $\gtrsim$30 s postburst, BAT light curve presents a tail of extended emission that we model with a simple power law until ∼240 s. This model yields $\alpha_\gamma = 0.936 \pm 0.015$ and $\chi^2/\mathrm{dof} = 2524/1112$ (see Figure 11). We notice that a broken power-law model does not increase the significance of the fit.

The GRB 190114C X-ray light curve has no shallow phase (see Yamazaki et al. 2019 for other GeV/TeV events) and decays as $\alpha_{\rm x} = 1.345 \pm 0.004$ through all *Swift* XRT observations (see Figure 11; $\chi^2/\mathrm{dof} = 1608/1052$), which is similar to the expected $\alpha_{\rm x} \sim 1.2$ decay for the normal spherical stage (Nousek et al. 2006; Zhang et al. 2006).

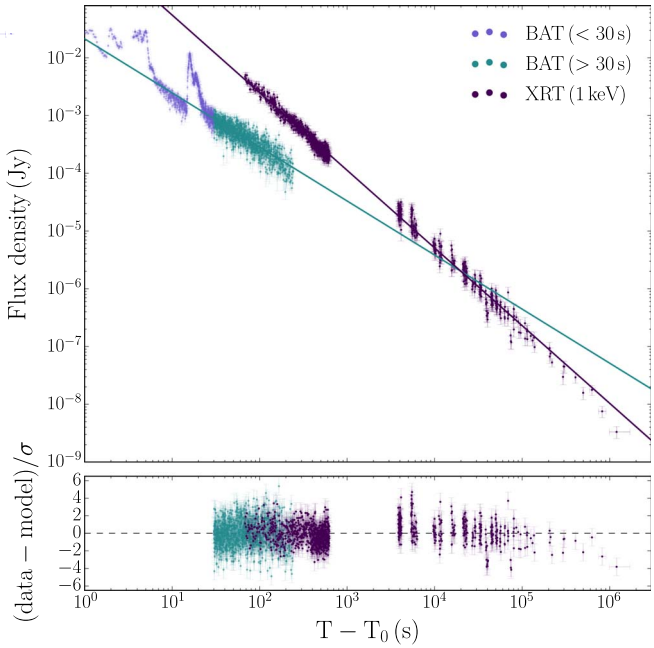

Figure 11. The GRB 190114C BAT/XRT emission (Evans et al. 2009) modeled in terms of power laws. The bottom panel corresponds to the residuals of the fit and T_0 to BAT trigger time.

However, Figure 11 late-time residuals show signs of a possible break, as the XRT light-curve model tends to overestimate the flux; the last two observation bins lay 2.6σ and 3.8σ away from the chosen model. To account for a possible change of the slope steepness during the late-time afterglow, we fit a broken power-law model that yields $\alpha_{\rm x1} = 1.321 \pm 0.005$, $\alpha_{\rm x2} = 1.49 \pm 0.02$, and a break time at $(1.8 \pm 0.3) \times 10^4$ s, with $\chi^2/\mathrm{dof} = 1530/1051$. This means a change of $\Delta\alpha_{\rm x} = 0.17 \pm 0.04$ in the temporal decay rate that does not have any spectral break associated; we exclude the passage of a break frequency. For GRB 090102

X-ray afterglow (see Table 4), Gendre et al. (2010) found a similar temporal break from $\alpha_1 = 1.29 \pm 0.03$ to $\alpha_2 = 1.48 \pm 0.10$ at a comparable time $1.9^{+1.5}_{-0.8} \times 10^4$ s and without any spectral change. Consequently, we explore the possibility of a jet break. From Sari et al.'s (1999) formulation, the jet opening angle is

$$\theta_j \approx 0.0297\left(\frac{t_j}{1\mathrm{hr}}\right)^{3/8}\left(\frac{E_{\rm iso}}{2.4 \times 10^{53}\mathrm{erg}}\right)^{-1/8}\left(\frac{1+z}{1.4245}\right)^{-3/8} \quad (1)$$

for an ISM-like environment and assuming typical values of circumburst density $n = 1$ cm^{-3} and radiative efficiency $\eta = 0.2$. Taking into account that the jet opening angle distribution of long GRBs peaks around 5.9° (Goldstein et al. 2016), $E_{\rm iso} = (2.4 \pm 0.5) \times 10^{53}$ erg (Frederiks et al. 2019), and $z = 0.4245 \pm 0.0005$ (Castro-Tirado et al. 2019), the jet break should be visible at $t_j \sim 10^5$ s. A jet break at $(1.8 \pm 0.3) \times 10^4$ s—implying $\theta_j \sim 3.1°$—is possible, and, given the scarcity of GCN observations around the break time, we cannot rule it out.

4.2.2. The Optical and X-Ray Afterglow

For pure forward shock emission in fireball model conditions, one would expect that if the optical and X-ray share the same spectral regime, the emission will decay at the same rate. Taking into account that $\alpha_{\rm opt,f} = 0.707 \pm 0.010$, $\alpha_{0.3-10\ \rm keV} = 1.345 \pm 0.004$, and $\alpha_{15-350\ \rm keV} = 0.936 \pm 0.015$, we find a difference of $\Delta\alpha_f = \alpha_x - \alpha_{\rm opt,f} = 0.638 \pm 0.011$ between the 0.3–10 keV/optical decay rates and $\Delta\alpha_f = 0.23 \pm 0.02$ for the 15–350 keV/optical emission, which implies that there is at least one break frequency between the X-ray and the optical. This interpretation is also supported by the need for a spectral break between these two bands that changes the slope by $\Delta\beta = 0.50 \pm 0.03$ (see Section 3.3.3).

For an ISM medium profile, slow cooling regime, and with the cooling frequency between the optical and X-ray bands, an electron index of $p \sim 1.95$ (see Section 4.1.1) implies spectral indexes of $\beta_{\rm opt,CR} \sim 0.48$ and $\beta_{\rm x,CR} \sim 0.98$, which are in agreement with $\beta_{\rm opt} = 0.43 \pm 0.02$ and $\beta_x = 0.93 \pm 0.02$ derived from the broadband SED modeling (see Section 3.3.3). The evolution of $E_{\rm break}$ for the last three SEDs is also consistent with the passage of the cooling frequency $\nu_c \propto t^{-\alpha_c}$ with $\alpha_c \sim 0.5$.

A difference of $\Delta\alpha_f = \pm 0.25$ is expected if the cooling frequency lies between the X-ray/optical bands. Taking into account that $\alpha_{\rm opt,f} = 0.707 \pm 0.010$, $\alpha_{15-350\ \rm keV} = 0.936 \pm 0.015$, and $\alpha_{80\rm keV-8\ MeV} = 0.99 \pm 0.05$ (Minaev & Pozanenko 2019), we find that the 15–350 keV/optical emission $\Delta\alpha_f = 0.23 \pm 0.02$ and the 80 keV–8 MeV/optical emission $\Delta\alpha_f = 0.28 \pm 0.05$ are consistent with $\Delta\alpha_f = \pm 0.25$. However, this relation does not hold for the 0.3–10 keV/optical emission with $\Delta\alpha_f = 0.638 \pm 0.011$. Furthermore, the steepness of the X-ray light curve $\alpha_{x,f} = 1.345 \pm 0.004$ implies a softer $\beta_{\rm x,CR} \sim 1.23$, $p_x \sim 2.46$, which does not agree with either the observed spectral indexes or the preferred model for the optical emission. Out of the 68 GRBs of Zaninoni et al.'s (2013) sample, only 19% of GRBs follow $\Delta\alpha_f = 0, \pm 0.25$ for all XRT X-ray/optical light-curve segments. The GRB 190114C belongs to the 41% of the GRB population for which no light-curve segments $\Delta\alpha_f$ satisfy the fireball model conditions for forward shock emission. Additionally, out of the six GRBs of Japelj et al.'s (2014) sample with reverse–forward shock signatures, only GRB 090424 fulfills $\Delta\alpha_f = 0, \pm 0.25$.

An alternative to reconcile the optical with the soft X-ray emission is to assume that they belong to two spatially or physically different processes. Supporting the scenario of complex jet structure or additional emission components, we have chromatic breaks that cannot be explained by either a break frequency crossing the band or an external density change (Oates et al. 2011). For example, a two-component jet would produce two forward shocks that would be responsible for, respectively, the optical and the X-ray emission at late times (GRB 050802, Oates et al. 2007; GRB 080319, Racusin et al. 2008).

5. Discussion

5.1. Strength of the Magnetic Fields in the Outflow

The reverse shock dynamics have mostly been studied for two regimes (Kobayashi 2000): the thick and thin shell. For the thick-shell regime, the initial Lorentz factor Γ is bigger than critical value Γ_c ($\Gamma > \Gamma_c$), and the reverse shock becomes relativistic in the unshocked material rest frame such that it effectively decelerates the shell. For the thin-shell regime ($\Gamma \lesssim \Gamma_c$), the reverse shock is subrelativistic and cannot effectively decelerate the shell. From Gomboc et al. (2008), the critical value is

$$\Gamma_c = 258\left(\frac{1+z}{1.4245}\right)^{3/8}\left(\frac{T}{30\ \mathrm{s}}\right)^{-3/8}\left(\frac{E_{\rm iso}}{2.4 \times 10^{53}\ \mathrm{erg}}\right)^{1/8} \quad (2)$$

for redshift 0.4245 ± 0.0005 (Castro-Tirado et al. 2019), $E_{\rm iso} = (2.4 \pm 0.5) \times 10^{53}$ erg (Frederiks et al. 2019), and prompt bulk emission duration $T = 30$ s and assuming $n = 1$ cm^{-3}.

Our interpretation for GRB 190114C optical afterglow is that the reverse shock peaks at the start of or before MASTER observations $\leqslant T_0 + 30$ s; the early-time observations from MASTER/RINGO3 and late-time GCNs are consistent with the reverse–forward shock model of Figure 9 (right); the detection of sub-TeV emission at $T_0 + 50$ s also supports an early afterglow peak, as it is thought to arise from external shocks (Derishev & Piran 2019; Mirzoyan 2019), and Ajello et al. (2020) suggested that the $\gtrsim T_0 + 10$ s emission already has an afterglow contribution. Because the optical afterglow is fading straight after the γ-ray prompt emission, GRB 190114C should be either in a thick or intermediate regime, $\Gamma \gtrsim \Gamma_c$. For $\Gamma \gg \Gamma_c$, the reverse shock emission should initially decay as $\alpha_r \sim 3$ because of the quick energy transfer by a rarefaction wave (Kobayashi & Sari 2000; Kobayashi & Zhang 2007), which is not in agreement with the observations. Consequently, Γ should be close to the critical value Γ_c, $\Gamma \sim \Gamma_c$; the reverse shock is marginally relativistic at the shock crossing time, and the thin-shell model is valid.

In order to quantify the strength of the magnetic field in the reverse shock region, Zhang et al. (2003) introduce the magnetic energy ratio R_B; this parameter is derived assuming different magnetic equipartition parameters for forward $\epsilon_{B,f}$ and reverse shock $\epsilon_{B,r}$ (the fireball ejecta might be endowed with primordial magnetic fields), no or moderate fireball magnetization (the magnetic fields do not affect the fireball dynamics), the same electron equipartition parameter ϵ_e and electron index p for both shock regions, the thin-shell regime, and the spectral

configuration $\nu_{\rm m,r} < \nu_{\rm m,f} < \nu_{\rm c,r} \leqslant \nu_{\rm c,f}$ at the shock crossing time. Additionally, we assume that the forward shock peaks during RINGO3 observations at $t_{\rm peak,f} \sim 900$ s, masked by reverse shock emission that decays as $\alpha_{\rm opt,r} = 1.711 \pm 0.012$, and that the reverse and forward shock emission are comparable at that time. Therefore, Gomboc et al. (2008) derived

$$R_{\rm B} \equiv \frac{\epsilon_{\rm B,r}}{\epsilon_{\rm B,f}} \sim [R_{\rm t}^{3}\Gamma^{(4\alpha_{\rm r}-7)}]^{2/(2\alpha_{\rm r}+1)}, \quad (3)$$

where $R_{\rm t}$ is the ratio between forward and reverse shock peak times $R_{\rm t} \equiv t_{\rm peak,f}/t_{\rm peak,r}$. Assuming $\Gamma \sim \Gamma_c$ and $t_{\rm peak,r} \sim 30$ s, we estimate that the magnetic energy density in the reverse shock region is higher than that in the forward shock region by a factor of $R_{\rm B} \sim 70$; the reverse shock emission could have globally ordered magnetic fields advected from the central engine.

Broadband afterglow modeling usually shows levels of $\epsilon_{\rm B,f} \sim 10^{-5} - 10^{-1}$ for the forward shock magnetic equipartition parameter (Panaitescu & Kumar 2002). For GRB 190114C, $\epsilon_{\rm B,f} \sim 10^{-5} - 10^{-4}$ (Ajello et al. 2020; Fraija et al. 2019b; Wang et al. 2019), so this GRB is likely weakly magnetized at the deceleration radius. Consequently, magnetic fields are dynamically subdominant, and bright reverse shock emission is expected (Zhang et al. 2003; Fan et al. 2004; Zhang & Kobayashi 2005). If $\epsilon_{\rm B,f} \sim 0.1$, as discussed in Derishev & Piran (2019), $\sigma_{\rm B}$ would be of order unity, and our model assumption (i.e., magnetic fields do not affect the dynamics of the outflow) becomes invalid. Although reconnections might be able to produce the prompt and early afterglow emission in the high-magnetization regime (e.g., Spruit et al. 2001; Lyutikov & Blandford 2003; Zhang & Yan 2011), our forward–reverse shock model (purely hydrodynamics model) can describe the early afterglow well, and we assume $\epsilon_{\rm B,f} \sim 10^{-5} - 10^{-4}$ as our fiducial value.

5.2. Maximum Reverse Shock SSC Energy

The maximum synchrotron energy that can be produced by shock-accelerated electrons is about $\nu'_{\rm max} \sim m_{\rm e}c^2/\alpha_{\rm FS} \sim 100$ MeV in the shock comoving frame, where $\alpha_{\rm FS}$ is the fine-structure constant. For the observer, this limit is boosted by the bulk Lorentz factor as $\nu_{\rm max} \sim 100\Gamma$ MeV $\sim 20(\Gamma/200)$ GeV. Since the bulk Lorentz factor is less than a few hundred in the afterglow phase, SSC processes are favored to explain the subteraelectronvolt emission (Ajello et al. 2020; Fraija et al. 2019a; Derishev & Piran 2019; Zhang et al. 2019; Ravasio et al. 2019; MAGIC Collaboration et al. 2019a, MAGIC Collaboration et al. 2019b).

Considering the longevity of the high-energy emission, the SSC emission is likely to originate from the forward shock region. As we discuss below, the maximal inverse Compton (IC) photon energy also favors the forward shock origin.

The typical random Lorentz factor of electrons in the reverse shock region is about $\gamma_{\rm m,r} \sim (\epsilon_{\rm e}/3)(m_{\rm p}/m_{\rm e}) \sim 20(\epsilon_{\rm e}/3 \times 10^{-2})$ at the onset of the afterglow, and it cools due to the adiabatic expansion of the shock ejecta as $\gamma_{\rm m,r} \propto t^{-2/7}$ (Kobayashi 2000). Since the typical value is lower by a factor of order Γ than that in the forward shock region, it is difficult to produce very high energy emission in the reverse shock region, even if a higher-order IC component is considered (Kobayashi et al. 2007). If the intermediate photon energy in the higher-order IC scattering (i.e., the photon energy before the scattering in the electron comoving frame) is too high, the Klein–Nishina effect suppresses the higher-order IC scattering. Since the intermediate photon energy can be as high as $\sim$100 keV ($\ll m_{\rm e}\,c^2$) and still be in the Thomson limit, the maximum IC energy is at most 100 $\gamma_{\rm m,r}\Gamma$ keV $\sim 3(\gamma_{\rm m,r}/100)(\Gamma/300)$ GeV. Basically, the same limit can be obtained by considering that electrons with a random Lorentz factor $\gamma_{\rm e}$ should be sufficiently energetic $\Gamma\gamma_{\rm e}m_{\rm e}c^2 \gg h\nu_{\rm IC}$ to upscatter a low-energy photon to a high-energy $h\nu_{\rm IC}$.

5.3. Structure of the Magnetic Fields in the Outflow

While the magnetization degree determines the strength of the magnetic field, GRB linear polarimetry directly informs the degree of ordered magnetic fields in the emitting region (e.g., length scales and geometry).

Theoretically, synchrotron emission can be up to 70% polarized (Rybicki & Lightman 1979), but this can be further reduced due to inhomogeneous magnetic fields (e.g., highly tangled magnetic fields or patches of locally ordered magnetic fields), a toroidal magnetic field viewed with a line of sight almost along the jet axis, the combination of several emission components endowed with ordered magnetic fields but with different polarization components (e.g., internal–external shocks), or the combination of reverse–forward shock emission. Additionally, if the reverse shock is propagating in a clumpy medium, polarization levels could also be reduced (Deng et al. 2017). If the emission region contains several independent patches of locally ordered magnetic fields, the degree and direction of polarization should depend on time, as the process is stochastic.

In Section 4.1, we have discussed that the steep-to-flat behavior of the GRB 190114C optical light curve is most likely due to a reverse–forward shock interplay. If the reverse shock emission is highly polarized, the degree of polarization should decline steadily as the unpolarized forward shock emerges (GRB 120308A; Mundell et al. 2013). In GRB 190114C, the reverse shock dominates the afterglow emission from 52 to 109 s postburst, and the polarization degree drops abruptly from $7.7\% \pm 1.1\%$ to $2.0^{+2.6}_{-1.5}\%$. From 200 to $\sim$2000 s postburst, the fraction of reverse to forward shock flux density declines from $\sim$0.96 to $\sim$0.31, and we detect a 2%–4% constant polarization degree in all three RINGO3 bands throughout this period. This contrasts with the higher value $P = 10\% \pm 1\%$ measured during the early light curve of GRB 090102 (Steele et al. 2009; Gendre et al. 2010), which shows a similar light-curve behavior of steep-to-flat decay typical of a combination of reverse and forward shock emission. At the polarization observing time, the modeling of GRB 090102 afterglow ($\alpha_{\rm r} = 1.987 \pm 0.012$, $t_{\rm peak,f} = 205 \pm 38$ s) indicates that the proportion of reverse to forward shock emission was $\sim$0.58, implying that the intrinsic polarization of the reverse shock emission is higher than observed (i.e., the ejecta contains large-scale ordered magnetic fields). The GRB 190114C polarization properties are also markedly different from those of GRB 120308A, in which the observed reverse shock emission is dominant and highly polarized ($28\% \pm 4\%$) at early times, decreasing to $16^{+5}_{-4}\%$ as the forward shock contribution increases with time.

In short, the polarization of the optical emission in GRB 190114C is unusually low, despite the clear presence of a reverse shock. We suggest the initial 7.7% ± 1.1% and sudden drop to $2.0^{+2.6}_{-1.5}$% may be due to a small contribution from optically polarized prompt photons (as for GRB 160625B; Troja et al. 2017), but therefore the dominant polarization degree of the afterglow is between 2% and 4% throughout. We next discuss possible scenarios to explain this low and constant 2%–4% degree.

5.3.1. Dust-induced Polarization: Low Intrinsic Polarization in the Emitting Region

Polarization measurements intrinsic to the afterglow are complicated by the fact that GRB 190114C is a highly extincted burst. Because of the preferred alignment of dust grains, dust in the line of sight can induce nonnegligible degrees of polarization that vectorially add to the intrinsic afterglow polarization; late-time polarimetric studies of GRB afterglows show few percents of polarization (e.g., Covino et al. 1999, 2004; Greiner et al. 2004; Wiersema et al. 2012). For the GRB 190114C line of sight, the polarization of the CD-27 1309 star, $P_{\{BV,R,I\}} = 0.3\% \pm 0.1\%, 0.1\% \pm 0.1\%, 0.3\% \pm 0.1\%$, gives an estimation of the polarization induced by Galactic dust. For the host galaxy, we estimate the dust-induced polarization degree with the Serkowski empirical relation (Serkowski et al. 1975; Whittet et al. 1992)

$$P = P_{\max} \exp\left[-K \ln^2\left(\frac{\lambda_{\max}}{\lambda}\right)\right], \quad (4)$$

where $\lambda_{\max}(\mu\mathrm{m}) = R_V/5.5$, $K = 0.01 \pm 0.05 + (1.66 \pm 0.09)\lambda_{\max}$, and $P_{\max} \lesssim 9\, E_{B-V}$. We introduce the redshifted host effect $\lambda_{\max} \longrightarrow (1+z)\lambda_{\max,\mathrm{HG}}$ (Klose et al. 2004; Wiersema et al. 2012), and we assume a Milky Way extinction profile with $E_{B-V,\mathrm{MW}} = 0.0124 \pm 0.0005$ (Schlegel et al. 1998) and an SMC profile for the host galaxy with $E_{B-V,\mathrm{HG}} = 0.51 \pm 0.04$. Taking into account the shape of the RINGO3 bandpasses, we find that the maximum polarization degree induced by the host galaxy dust is $P_{\{BV,R,I\}} \lesssim 3.9\%, 4.5\%, 4.5\%$, compatible with the constant 2%–4% polarization degree of the GRB detected since 109 s postburst.

Depending on the relative position of the polarization vectors (the alignment of dust grains to the intrinsic polarization vector of the ejecta), dust could either polarize or depolarize the outflow. If dust was depolarizing the intrinsic polarization, this would mean a gradual rotation of the angle as the percentage of polarized reverse shock photons decreases. The constant angle and polarization degree favor the interpretation that the ∼2%–4% ordered component is compatible with dust-induced levels (see Figure 5); i.e., the intrinsic polarization at that time is very low or negligible.

5.3.2. Distortion of the Large-scale Magnetic Fields

Although the early afterglow modeling implies that the ejecta from the central engine is highly magnetized for this event, the polarization degree of the reverse shock emission is very low, and the 2%–4% polarization signal is likely to be induced by dust. This is in contrast to the high polarization signals observed in other GRB reverse shock emission (GRB 090102, Steele et al. 2009; GRB 101112A, Steele et al. 2017; GRB 110205A, Steele et al. 2017, GRB 120308A, Mundell et al. 2013).

One possibility is that the low degree of polarization arises from other emission mechanisms in addition to synchrotron emission. Since the optical depth of the ejecta is expected to be well below unity at the onset of afterglow, most synchrotron photons from the reverse shock are not affected by IC scattering processes (the cooling of electrons is also not affected if the Compton y-parameter is small). The polarization degree of the synchrotron emission does not change even if the IC scattering is taken into account. However, the polarization degree is expected to be reduced for the photons upscattered by random electrons (i.e., SSC photons; Lin et al. 2017). We now consider whether this can explain the observed low polarization degree of the reverse shock emission.

If the typical frequency of the forward shock emission is in the optical band $\nu_{\mathrm{m,f}} \sim 5 \times 10^{14}$ Hz at $t \sim 900$ s, as our afterglow modeling suggests (right panel of Figure 9), it should be about $\nu_{\mathrm{m,f}} \sim 8 \times 10^{16}$ Hz at the onset of afterglow ($t_{\mathrm{d}} \sim 30$ s). Since the typical frequency of the reverse shock emission is lower by a factor of $\sim\Gamma^2$ (this factor weakly depends on the magnetization parameter R_{B}, but the inclusion of a correction factor does not change our conclusion; see Harrison & Kobayashi 2013 for more details), it is about $\nu_{\mathrm{m,r}} \sim 10^{12}$ Hz at that time for $\Gamma \sim \Gamma_{\mathrm{c}} = 260$. Assuming a random Lorentz factor of electrons in the reverse shock region $\gamma_{\mathrm{m,r}} \sim 20(\epsilon_{\mathrm{e}}/3 \times 10^{-2})$, the typical frequency of the first SSC emission is in the optical band $\nu^{\mathrm{IC}}_{\mathrm{m,r}} \sim \gamma^2_{\mathrm{m,r}}\nu_{\mathrm{m,r}} \sim 5 \times 10^{14}$ Hz.

The optical depth of the ejecta at the onset of afterglow is given by $\tau = \sigma_{\mathrm{T}} N_{\mathrm{e}}/4\pi R_{\mathrm{d}}^2 \sim (\sigma_{\mathrm{T}}/3)\Gamma n R_{\mathrm{d}} \sim 7 \times 10^{-6} n$, where σ_{T} is the Thomson cross section, N_{e} is the number of electrons in the ejecta, $R_{\mathrm{d}} \sim 2\, c\Gamma^2 t_{\mathrm{d}} \sim 10^{17}$ cm is the deceleration radius, and we have used the fact that the mass of the ejecta is larger by a factor of Γ than that of the ambient material swept by the shell at the deceleration time. The spectral peak power of the first SSC emission is roughly given by $F^{\mathrm{IC}}_{\max} \sim \tau F_{\max,\mathrm{r}}$, where $F_{\max,\mathrm{r}}$ is the spectral peak power of the reverse shock synchrotron emission (e.g., Kobayashi et al. 2007). The ratio of the contributions from the first SSC and the synchrotron emission to the optical band is about $\tau F_{\max,\mathrm{r}}/(F_{\max,\mathrm{r}}(\nu_{\mathrm{opt}}/\nu_{\mathrm{m,r}})^{-(p-1)/2}) \sim \tau(\nu_{\mathrm{opt}}/\nu_{\mathrm{m,r}})^{1/2} \sim 7 \times 10^{-6} n$ at the onset of the afterglow. Since the synchrotron emission dominates the optical band, the IC process does not explain the low polarization degree.

Consequently, we suggest that GRB 190114C large-scale ordered magnetic fields could have been largely distorted on timescales previous to reverse shock emission (see also GRB 160625B; Troja et al. 2017). We speculate that the detection of bright prompt and afterglow emission from teraelectronvolt to radio wavelengths in GRB 190114C, coupled with the low degree of observed optical polarization, may be explained by the catastrophic/efficient dissipation of magnetic energy from and consequent destruction of the order in the primordial magnetic fields of the outflow, e.g., via turbulence and reconnection at prompt emission timescales (ICMART; Zhang & Yan 2011; Deng et al. 2015, 2016; Bromberg & Tchekhovskoy 2016). For GRB 190114C, reconnection could be a mechanism for the production of the high-energy *Fermi*-LAT photons that exceed the maximum synchrotron energy (another possibility is SSC; Ajello et al. 2020). If the 7.7% ± 1.1% detection at 52 ± 6 s postburst is interpreted as due to a residual contribution from polarized prompt photons

(as in GRB 160625B; Troja et al. 2017), this would further support the existence of ordered magnetic fields close to prompt emission timescales and their consequent destruction for reverse shock emission.

The sample of high-quality early-time polarimetric observations of GRB afterglows remains small (<10), and for prompt emission, it is smaller still (2). Future high-quality early-time polarimetric observations at optical and other wavelengths are vital to determine the intrinsic properties of GRB magnetic fields and their role in GRB radiation emission mechanisms.

6. Conclusions

The early-time optical observations of GRB 190114C afterglow yield an important constraint on the shock evolution and the interplay between reverse and forward shock emission. The steep-to-flat light-curve transition favors the presence of reverse shock emission, with the forward shock peaking during RINGO3 observations.

The forward–reverse shock modeling suggests that the microscopic parameter ϵ_B is higher by a factor of $\sim$70 in the reverse shock than in the forward shock region. It indicates that the fireball ejecta is endowed with the primordial magnetic fields from the central engine. Since we have successfully modeled the early afterglow in the forward–reverse shock framework, the outflow is likely to be baryonic rather than Poynting flux–dominated at the deceleration radius.

The GRB 190114C polarization degree undergoes a sharp drop from $7.7\% \pm 1.1\%$ to $2.0^{+2.6}_{-1.5}\%$ 52–109 s postburst, inconsistent with pure reverse shock emission; we suggest a contribution from prompt photons. Later on, multiband polarimetry also shows a constant $P = 2\%$–4% polarization degree during the reverse–forward shock interplay consistent with dust-induced levels from the highly extincted host galaxy. The low intrinsic polarization signal is in contrast to the $P > 10\%$ measured previously for the events that show a signature of reverse shock emission (i.e., steep rise or decay). Forward shock SSC emission is favored for the origin of the long-lasting sub-TeV emission (we have shown that reverse shock SSC is not energetic enough to produce the sub-TeV emission). We have also tested whether reverse shock SSC emission can explain the low optical polarization degree; the polarization degree of the photons upscattered by random electrons would be lower than that of the synchrotron photons. Since we show that the first SSC component in the optical band is masked by the synchrotron component, the IC process does not explain the low polarization degree. Instead, the unexpectedly low intrinsic polarization degree in GRB 190114C can be explained if large-scale jet magnetic fields are distorted on timescales prior to reverse shock emission.

A larger, statistical sample of early-time polarization measurements with multiwavelength information is required to understand the timescales and mechanisms that cause distortion of the large-scale ordered magnetic fields and ultimately constrain jet models.

We thank the anonymous referee for a constructive report that improved the quality of our paper. The Liverpool Telescope is operated on the island of La Palma by Liverpool John Moores University in the Spanish Observatorio del Roque de los Muchachos of the Instituto de Astrofisica de Canarias with financial support from the UK Science and Technology Facilities Council. MASTER is supported in part by the development program of Lomonosov Moscow State University (equipment) by RFBR grant 19-29-11011. This work made use of data supplied by the UK *Swift* Science Data Centre at the University of Leicester. The research leading to these results received funding from the European Union's Horizon 2020 Programme under the AHEAD project (grant agreement 654215). N.J. and C.G.M. acknowledge financial support from Mr Jim Sherwin and Mrs Hiroko Sherwin. C.G.M. acknowledges support from the Science and Technology Facilities Council and the UK Research and Innovation (ST/N001265/1). C.G. acknowledges support for this work provided by Università di Ferrara through grant FIR 2018 "A Broad-band study of Cosmic Gamma-ray Burst Prompt and Afterglow Emission." A.G. acknowledges financial support from the Slovenian Research Agency (grants P1-0031, I0-0033, and J1-8136) and networking support by the COST Actions CA16104 GWverse and CA16214 PHAROS. D.A.H.B. acknowledges research support from the South African National Research Foundation. N.B. was supported by RFBR BRICS grant 17-52-80133 and the Russian Federation Ministry of Science and High Education (agreement No. 075-15-2019-1631).

Software: Matplotlib (Hunter 2007), SciPy (Virtanen et al. 2019), PyFITS (Barrett & Bridgman 1999), Astropy Photutils (Bradley et al. 2016), Astroalign (Beroiz et al. 2019), XSPEC and PyXSPEC (v. 12.9.1; Arnaud et al. 1999), HEAsoft (v6.22.1; Blackburn 1995).

ORCID iDs

N. Jordana-Mitjans https://orcid.org/0000-0002-5467-8277
C. G. Mundell https://orcid.org/0000-0003-2809-8743
S. Kobayashi https://orcid.org/0000-0001-7946-4200
R. J. Smith https://orcid.org/0000-0003-3434-1922
C. Guidorzi https://orcid.org/0000-0001-6869-0835
I. A. Steele https://orcid.org/0000-0001-8397-5759
M. Shrestha https://orcid.org/0000-0002-4022-1874
A. Gomboc https://orcid.org/0000-0002-0908-914X
M. Marongiu https://orcid.org/0000-0002-5817-4009
R. Martone https://orcid.org/0000-0002-0335-319X
V. Lipunov https://orcid.org/0000-0003-3668-1314
D. A. H. Buckley https://orcid.org/0000-0002-7004-9956
R. Rebolo https://orcid.org/0000-0003-3767-7085
N. M. Budnev https://orcid.org/0000-0002-2104-6687

References

Abbott, B., Abbott, R., Abbott, T., et al. 2017a, ApJL, 848, L12
Abbott, B. P., Abbott, R., Abbott, T. D., et al. 2017b, PhRvL, 119, 161101
Ajello, M., Arimoto, M., Axelsson, M., et al. 2020, ApJ, 890, 9
Alexander, K. D., Laskar, T., Berger, E., Mundell, C. G., & Margutti, R. 2019, GCN, 23726, 1
Arnaud, K., Dorman, B., & Gordon, C. 1999, XSPEC: An X-ray spectral fitting package v12.9.1, Astrophysics Source Code Library, ascl:9910.005
Arnold, D. 2017, PhD thesis, Liverpool John Moores Univ. 10.24377/LJMU.t.00006687
Arnold, D. M., Steele, I. A., Bates, S. D., Mottram, C. J., & Smith, R. J. 2012, Proc. SPIE, 8446, 84462J
Barrett, P. E., & Bridgman, W. T. 1999, in ASP Conf. Ser. 172, PyFITS, a FITS Module for Python, ed. D. M. Mehringer, R. L. Plante, & D. A. Roberts (San Francisco, CA: ASP), 483
Barthelmy, S. D., Barbier, L. M., Cummings, J. R., et al. 2005, SSRv, 120, 143
Beardmore, A. 2019, GCN, 23736, 1
Berger, E. 2014, ARA&A, 52, 43
Beroiz, M., Cabral, J. B., & Sanchez, B. 2019, arXiv:1909.02946
Bessell, M., & Murphy, S. 2012, PASP, 124, 140

Bikmaev, I., Irtuganov, E., Sakhibullin, N., et al. 2019, GCN, 23766, 1
Blackburn, J. K. 1995, in ASP Conf Ser. 77, FTOOLS: A FITS Data Processing and Analysis Software Package, ed. R. A. Shaw, H. E. Payne, & J. J. E. Hayes (San Francisco, CA: ASP), 367
Bohlin, R. C., Gordon, K. D., & Tremblay, P. E. 2014, PASP, 126, 711
Bolmer, J., & Schady, P. 2019, GCN, 23702, 1
Bradley, L., Sipocz, B., Robitaille, T., et al. 2016, Photutils: Photometry Tools v0.4, Astrophysics Source Code Library, ascl:1609.011
Bromberg, O., & Tchekhovskoy, A. 2016, MNRAS, 456, 1739
Castro-Tirado, A. J., Hu, Y., Fernandez-Garcia, E., et al. 2019, GCN, 23708, 1
Chambers, K. C., Magnier, E. A., Metcalfe, N., et al. 2016, arXiv:1612.05560
Cherukuri, S. V., Jaiswal, V., Misra, K., et al. 2019, GCN, 23762, 1
Clarke, D., & Neumayer, D. 2002, A&A, 383, 360
Covino, S., Campana, S., Conciatore, M. L., et al. 2010, A&A, 521, A53
Covino, S., Ghisellini, G., Lazzati, D., & Malesani, D. 2004, in ASP Conf. Series 312, Gamma-Ray Bursts in the Afterglow Era, ed. M. Feroci et al. (San Francisco, CA: ASP), 169
Covino, S., Lazzati, D., Ghisellini, G., et al. 1999, A&A, 348, L1
Cucchiara, A., Cenko, S. B., Bloom, J. S., et al. 2011, ApJ, 743, 154
D'Avanzo, P. 2019, GCN, 23754, 1
D'Elia, V., D'Ai, A., Sbarufatti, B., et al. 2019, GCN, 23706, 1
Deng, W., Li, H., Zhang, B., & Li, S. 2015, ApJ, 805, 163
Deng, W., Zhang, B., Li, H., & Stone, J. M. 2017, ApJL, 845, L3
Deng, W., Zhang, H., Zhang, B., & Li, H. 2016, ApJL, 821, L12
Derishev, E., & Piran, T. 2019, ApJL, 880, L27
Evans, P. A., Beardmore, A. P., Page, K. L., et al. 2009, MNRAS, 397, 1177
Fan, Y. Z., Wei, D. M., & Wang, C. F. 2004, A&A, 424, 477
Fox, D. W., Price, P. A., Soderberg, A. M., et al. 2003, ApJL, 586, L5
Fraija, N., Barniol Duran, R., Dichiara, S., & Beniamini, P. 2019a, ApJ, 883, 162
Fraija, N., Dichiara, S., Pedreira, A. C. C. d. E. S., et al. 2019b, ApJL, 879, L26
Frederiks, D., Golenetskii, S., Aptekar, R., et al. 2019, GCN, 23737, 1
Gao, H., Lei, W.-H., Zou, Y.-C., Wu, X.-F., & Zhang, B. 2013, NewAR, 57, 141
Gendre, B., Klotz, A., Palazzi, E., et al. 2010, MNRAS, 405, 2372
Ghisellini, G., & Lazzati, D. 1999, MNRAS, 309, L7
Giannios, D., Mimica, P., & Aloy, M. A. 2008, A&A, 478, 747
Goldstein, A., Connaughton, V., Briggs, M. S., & Burns, E. 2016, ApJ, 818, 18
Gomboc, A., Kobayashi, S., Guidorzi, C., et al. 2008, ApJ, 687, 443
Gorbovskoy, E., Ivanov, K., Lipunov, V., et al. 2010, AdAst, 2010, 917584
Gorbovskoy, E. S., Lipunov, V. M., Buckley, D. A. H., et al. 2016, MNRAS, 455, 3312
Granot, J., & Königl, A. 2003, ApJL, 594, L83
Greiner, J., Klose, S., Reinsch, K., et al. 2004, in AIP Conf. Proc. 727, Gamma-Ray Bursts: 30 Years of Discovery, ed. E. Fenimore & M. Galassi (Melville, NY: AIP), 269
Gropp, J. D., Kennea, J. A., Klingler, N. J., et al. 2019, GCN, 23688, 1
Guidorzi, C., Monfardini, A., Gomboc, A., et al. 2006, PASP, 118, 288
Haislip, J. B., Nysewander, M. C., Reichart, D. E., et al. 2006, Natur, 440, 181
Hamburg, R., Veres, P., Meegan, C., et al. 2019, GCN, 23707, 1
Harrison, R., & Kobayashi, S. 2013, ApJ, 772, 101
Hunter, J. D. 2007, CSE, 9, 90
Im, M., Paek, G. S., Kim, S., Lim, G., & Choi, C. 2019a, GCN, 23717, 1
Im, M., Paek, G. S. H., & Choi, C. 2019b, GCN, 23757, 1
Izzo, L., Noschese, A., D'Avino, L., & Mollica, M. 2019, GCN, 23699, 1
Japelj, J., Kopač, D., Kobayashi, S., et al. 2014, ApJ, 785, 84
Jin, Z.-P., Covino, S., Della Valle, M., et al. 2013, ApJ, 774, 114
Johnson, H., & Morgan, W. 1953, ApJ, 117, 313
Kim, J., & Im, M. 2019, GCN, 23732, 1
Kim, J., Im, M., Lee, C. U., et al. 2019, GCN, 23734, 1
Klose, S., Palazzi, E., Masetti, N., et al. 2004, A&A, 420, 899
Kobayashi, S. 2000, ApJ, 545, 807
Kobayashi, S., & Sari, R. 2000, ApJ, 542, 819
Kobayashi, S., & Zhang, B. 2003a, ApJL, 582, L75
Kobayashi, S., & Zhang, B. 2003b, ApJ, 597, 455
Kobayashi, S., & Zhang, B. 2007, ApJ, 655, 973
Kobayashi, S., Zhang, B., Mészáros, P., & Burrows, D. 2007, ApJ, 655, 391
Kocevski, D., Omodei, N., Axelsson, M., et al. 2019, GCN, 23709, 1
Kornilov, V. G., Lipunov, V. M., Gorbovskoy, E. S., et al. 2012, ExA, 33, 173
Krimm, H. A., Barthelmy, S. D., Cummings, J. R., et al. 2019, GCN, 23724, 1
Kumar, B., Pandey, S. B., Singh, A., et al. 2019a, GCN, 23742, 1
Kumar, H., Srivastav, S., Waratkar, G., et al. 2019b, GCN, 23733, 1
Laskar, T., Alexander, K. D., Berger, E., et al. 2019a, GCN, 23728, 1
Laskar, T., Alexander, K. D., Gill, R., et al. 2019b, ApJL, 878, L26
Li, L., Wang, Y., Shao, L., et al. 2018, ApJS, 234, 26
Lin, H.-N., Li, X., & Chang, Z. 2017, ChPhC, 41, 045101
Lipunov, V., Kornilov, V., Gorbovskoy, E., et al. 2010, AdAst, 2010, 349171
Lyutikov, M., & Blandford, R. 2003, arXiv:astro-ph/0312347
Lyutikov, M., Pariev, V. I., & Blandford, R. D. 2003, ApJ, 597, 998
MAGIC Collaboration, Acciari, V. A., Ansoldi, S., et al. 2019a, Natur, 575, 455
MAGIC Collaboration, Acciari, V. A., Ansoldi, S., et al. 2019b, Natur, 575, 459
Mazaeva, E., Pozanenko, A., Volnova, A., Belkin, S., & Krugov, M. 2019a, GCN, 23741, 1
Mazaeva, E., Pozanenko, A., Volnova, A., Belkin, S., & Krugov, M. 2019b, GCN, 23746, 1
Mazaeva, E., Pozanenko, A., Volnova, A., Belkin, S., & Krugov, M. 2019c, GCN, 23787, 1
Medvedev, M. V., & Loeb, A. 1999, ApJ, 526, 697
Melandri, A., Izzo, L., D'Avanzo, P., et al. 2019, GCN, 23983, 1
Melandri, A., Mundell, C. G., Kobayashi, S., et al. 2008, ApJ, 686, 1209
Mészáros, P. 2002, ARA&A, 40, 137
Minaev, P., & Pozanenko, A. 2019, GCN, 23714, 1
Mirzoyan, R. 2019, ATel, 12390, 1
Morgan, A. N., Perley, D. A., Cenko, S. B., et al. 2014, MNRAS, 440, 1810
Mundell, C. G., Kopač, D., Arnold, D. M., et al. 2013, Natur, 504, 119
Mundell, C. G., Steele, I. A., Smith, R. J., et al. 2007, Sci, 315, 1822
Nousek, J. A., Kouveliotou, C., Grupe, D., et al. 2006, ApJ, 642, 389
Oates, S. R., de Pasquale, M., Page, M. J., et al. 2007, MNRAS, 380, 270
Oates, S. R., Page, M. J., Schady, P., et al. 2011, MNRAS, 412, 561
Panaitescu, A., & Kumar, P. 2002, ApJ, 571, 779
Pandey, S. B., Swenson, C. A., Perley, D. A., et al. 2010, ApJ, 714, 799
Pei, Y. C. 1992, ApJ, 395, 130
Perley, D. A., Bloom, J. S., Butler, N. R., et al. 2008, ApJ, 672, 449
Perna, R., Lazzati, D., & Fiore, F. 2003, ApJ, 585, 775
Piran, T. 1999, PhR, 314, 575
Piran, T. 2004, RvMP, 76, 1143
Planck Collaboration, Aghanim, N., Akrami, Y., et al. 2018, arXiv:1807.06209
Racusin, J. L., Karpov, S. V., Sokolowski, M., et al. 2008, Natur, 455, 183
Racusin, J. L., Liang, E. W., Burrows, D. N., et al. 2009, ApJ, 698, 43
Ragosta, F., Olivares, F., D'Avanzo, P., et al. 2019, GCN, 23748, 1
Ravasio, M. E., Oganesyan, G., Salafia, O. S., et al. 2019, A&A, 626, A12
Rees, M. J., & Meszaros, P. 1994, ApJL, 430, L93
Rizzuto, D., Guidorzi, C., Romano, P., et al. 2007, MNRAS, 379, 619
Rybicki, G. B., & Lightman, A. P. 1979, Radiative Processes in Astrophysics (Weinheim: Wiley VCH)
Sari, R. 1999, ApJL, 524, L43
Sari, R., & Piran, T. 1999, ApJ, 520, 641
Sari, R., Piran, T., & Halpern, J. P. 1999, ApJL, 519, L17
Sari, R., Piran, T., & Narayan, R. 1998, ApJL, 497, L17
Schlegel, D. J., Finkbeiner, D. P., & Davis, M. 1998, ApJ, 500, 525
Schulze, S., Anderson, G., Moin, A., et al. 2019, GCN, 23745, 1
Selsing, J., Fynbo, J. P. U., Heintz, K. E., & Watson, D. 2019, GCN, 23695, 1
Serkowski, K., Mathewson, D. S., & Ford, V. L. 1975, ApJ, 196, 261
Shao, L., & Dai, Z. G. 2005, ApJ, 633, 1027
Siegel, M. H., & Gropp, J. D. 2019, GCN, 23725, 1
Simmons, J. F. L., & Stewart, B. G. 1985, A&A, 142, 100
Singh, A., Kumar, B., Sahu, D. K., et al. 2019, GCN, 23798, 1
Słowikowska, A., Krzeszowski, K., Żejmo, M., Reig, P., & Steele, I. 2016, MNRAS, 458, 759
Spruit, H. C., Daigne, F., & Drenkhahn, G. 2001, A&A, 369, 694
Steele, I. A., Kopač, D., Arnold, D. M., et al. 2017, ApJ, 843, 143
Steele, I. A., Mundell, C. G., Smith, R. J., Kobayashi, S., & Guidorzi, C. 2009, Natur, 462, 767
Steele, I. A., Smith, R. J., Rees, P. C., et al. 2004, Proc. SPIE, 5489, 679
Tremou, L., Heywood, I., Vergani, S. D., et al. 2019, GCN, 23760, 1
Troja, E., Lipunov, V. M., Mundell, C. G., et al. 2017, Natur, 547, 425
Ursi, A., Tavani, M., Marisaldi, M., et al. 2019, GCN, 23712, 1
Usov, V. V. 1994, MNRAS, 267, 1035
Vestrand, W. T., Wren, J. A., Panaitescu, A., et al. 2014, Sci, 343, 38
Virtanen, P., Gommers, R., Oliphant, T. E., et al. 2019, arXiv:1907.10121
Volvach, A. E., Volvach, L. N., & Pozanenko, A. 2019, GCN, 23750, 1
Wald, A., & Wolfowitz, J. 1940, Ann. Math. Stat., 11, 147
Wang, X.-Y., Liu, R.-Y., Zhang, H.-M., Xi, S.-Q., & Zhang, B. 2019, ApJ, 884, 117
Watson, A. M., Butler, N., Kutyrev, A., et al. 2019, GCN, 23751, 1
Wei, D. M., Yan, T., & Fan, Y. Z. 2006, ApJL, 636, L69
Whittet, D. C. B., Martin, P. G., Hough, J. H., et al. 1992, ApJ, 386, 562
Wiersema, K., Curran, P. A., Krühler, T., et al. 2012, MNRAS, 426, 2

Willingale, R., Starling, R. L. C., Beardmore, A. P., Tanvir, N. R., & O'Brien, P. T. 2013, MNRAS, 431, 394
Woosley, S. E. 1993, ApJ, 405, 273
Xiao, S., Li, C. K., Li, X. B., et al. 2019, GCN, 23716, 1
Yamazaki, R., Sato, Y., Sakamoto, T., & Serino, M. 2019, arXiv:1910.04097
Zaninoni, E., Bernardini, M. G., Margutti, R., Oates, S., & Chincarini, G. 2013, A&A, 557, A12
Zhang, B., Fan, Y. Z., Dyks, J., et al. 2006, ApJ, 642, 354
Zhang, B., & Kobayashi, S. 2005, ApJ, 628, 315
Zhang, B., Kobayashi, S., & Mészáros, P. 2003, ApJ, 595, 950
Zhang, B., & Mészáros, P. 2004, IJMPA, 19, 2385
Zhang, B., & Yan, H. 2011, ApJ, 726, 90
Zhang, H., Christie, I., Petropoulou, M., Rueda-Becerril, J. M., & Giannios, D. 2019, arXiv:1910.14049